Journal of
Composites Science

MDPI

Article

Composite Materials Based on Bioresorbable Polymers and Phosphate Phases for Bone Tissue Regeneration

Oana Maria Caramidaru [1], Celina Maria Damian [2], Gianina Popescu-Pelin [3], Mihaela Bacalum [4], Roberta Moisa [4], Cornelia-Ioana Ilie [5,6], Sorin-Ion Jinga [1] and Cristina Busuioc [5,6,*]

[1] Faculty of Medical Engineering, National University of Science and Technology Politehnica Bucharest, RO-011061 Bucharest, Romania
[2] Advanced Polymer Materials Group, National University of Science and Technology Politehnica Bucharest, RO-011061 Bucharest, Romania
[3] National Institute for Laser, Plasma and Radiation Physics, RO-077125 Magurele, Romania
[4] Horia Hulubei National Institute of Physics and Nuclear Engineering, RO-077125 Magurele, Romania
[5] Faculty of Chemical Engineering and Biotechnology, National University of Science and Technology Politehnica Bucharest, RO-011061 Bucharest, Romania
[6] National Center of Micro and Nanomaterials, National University of Science and Technology Politehnica Bucharest, RO-060042 Bucharest, Romania
* Correspondence: cristina.busuioc@upb.ro

Abstract

Bone tissue plays a vital role in the human body and possesses intrinsic self-repair mechanisms; however, large defects or pathological fractures may exceed its natural healing capacity. Bone tissue engineering provides promising strategies to restore bone integrity through the use of scaffolds, growth factors, and stem cells. While calcium phosphate (CaP)-based ceramics, such as hydroxyapatite (HAp) and tricalcium phosphate (TCP), represent the current benchmark, their limitations, including slow degradation (HAp) and limited osteoinductivity (TCP), have driven the development of alternative biomaterials. In this context, magnesium phosphate (MgP)-based materials have gained increasing attention due to their tunable resorption rate, improved biodegradability, and ability to stimulate osteogenesis and angiogenesis through the release of magnesium (Mg^{2+}) ions. This study reports on composite scaffolds based on electrospun poly(ε-caprolactone) (PCL) fibres coated with MgP layers doped with lithium (Li) and zinc (Zn), designed to mimic the nanofibrous architecture of the extracellular matrix. Lithium and zinc were selected due to their known ability to modulate cellular response, with lithium promoting osteogenic activity and zinc contributing to improved cell proliferation and antibacterial potential. The phosphate phases obtained by coprecipitation were deposited onto the PCL fibres using Matrix-Assisted Pulsed Laser Evaporation (MAPLE), enabling controlled surface functionalization. Following thermal treatment, the formation of the crystalline magnesium pyrophosphate ($Mg_2P_2O_7$) phase was confirmed by chemical and structural characterization. The combination of a slowly degrading PCL matrix, providing sustained structural support, and a bioactive MgP coating, enabling rapid and controlled ion release, results in improved scaffold performance in terms of biocompatibility, biodegradability, and bioactivity. While the slow degradation rate of PCL ensures mechanical stability over an extended period, the surface-deposited MgP phase allows immediate interaction with the biological environment, facilitating faster ion release and enhancing cell–material interactions. These findings highlight the potential of the developed composites as promising candidates for trabecular bone regeneration and as viable alternatives to conventional CaP-based scaffolds in regenerative medicine.

Check for updates

Academic Editors: Luis Jesús Villarreal-Gómez, Yoxkin Estévez-Martínez and Faruk Fonthal Rico

Received: 19 March 2026
Revised: 15 April 2026
Accepted: 21 April 2026
Published: 23 April 2026

Copyright: © 2026 by the authors. Licensee MDPI, Basel, Switzerland. This article is an open access article distributed under the terms and conditions of the Creative Commons Attribution (CC BY) license.

Keywords: polycaprolactone; magnesium phosphate; fibres; composite materials; extracellular matrix; bone tissue engineering

1. Introduction

Regenerative medicine is an interdisciplinary field applying principles from engineering and life sciences to restore or replace damaged tissues and organs. Bone tissue regeneration represents a major challenge in regenerative medicine, particularly in the treatment of bone defects caused by trauma, degenerative diseases (e.g., osteoporosis), or surgical interventions [1,2]. Unlike other tissue types, bone has the ability to self-repair, often healing lesions and fractures without forming scars. However, in cases of pathological fractures, trauma, or extensive bone defects, the healing process can fail. Tissue engineering therefore represents the ultimate solution for treating bone loss, especially in elderly patients. A critical aspect is designing materials that mimic the extracellular matrix, guiding cellular behaviour, supporting tissue formation, and enabling controlled delivery of bioactive factors to facilitate natural healing processes [3,4].

Addressing this challenge involves replacing traditional methods, such as metal prostheses or bone grafts, with polymeric composite materials that provide high flexibility, elasticity, and biodegradability to stimulate the body natural regeneration processes. Scaffolds play a crucial role in supporting osteogenesis, providing structural support and guiding tissue regeneration. Bioresorbable polymers, such as polylactic acid (PLA) and polycaprolactone (PCL), are frequently used due to their biocompatibility, controlled biodegradability, and mechanical properties. While synthetic polymers offer numerous benefits, their regenerative capacity is often lower than natural polymers, prompting the development of composite materials that combine polymers with bioactive ceramics or other inorganic phases to enhance osteoconductivity and bioresorbability [5–7].

Phosphate-based materials are used as bone substitutes due to their ability to replicate the natural structure of bone, promoting osteoblast development and accelerating osteogenesis. Hydroxyapatite (HAP) and tricalcium phosphate (TCP) are the most common synthetic ceramic bone substitutes; however, TCP degrades more easily in vivo and has limited osteoinductivity. To overcome these limitations, magnesium phosphate (MgP)-based bioceramics have been developed. MgP offers good mechanical strength and an adjustable resorption rate compared to CaP ceramics. It provides high bioactivity, stimulates cell adhesion and proliferation, enhances mineralization of the bone matrix, and gradually releases essential ions involved in osteogenesis [8–11]. Moreover, magnesium (Mg^{2+}) is a naturally occurring element in the human body, the second most abundant intracellular cation after potassium (K^{+}), and plays a crucial role in physiological bone mineralization [12]. Additionally, MgP promotes angiogenesis and supports osteoblast differentiation, contributing to bone formation around the implant [9].

Doping MgP with certain elements, such as strontium (Sr^{2+}), zinc (Zn^{2+}) and lithium (Li^{+}), enhances its biological properties and therapeutic potential for bone regeneration. Strontium has been shown to stimulate osteoblast differentiation and inhibit osteoclast activity, promoting bone formation [13]. Zinc supports osteoblast proliferation, improves mechanical properties, and provides antibacterial effects [14], while lithium promotes osteogenesis and angiogenesis, enhancing both cell proliferation and scaffold stability [15].

While the beneficial effects of zinc and lithium doping are well established, their biological response is strongly concentration dependent. In particular, low-to-moderate zinc concentrations (typically ~1–5%) [16–18] have been associated with enhanced cell

proliferation and cytocompatibility, whereas higher concentrations (≥10%) [16] may induce cytotoxic effects. Similarly, lithium exhibits a concentration dependent behaviour, with lower to moderate levels being preferred to maintain biocompatibility, while excessive concentrations may negatively affect cellular response [19]. Therefore, the selection of dopant levels must ensure a balance between bioactivity and biocompatibility. In addition to lithium and zinc, other dopants such as silver (Ag^+) and copper (Cu^{2+}) have also been reported in the literature [20,21] mainly for their antibacterial, pro-angiogenic effects and suitability for bone regeneration applications.

MgP is commonly synthesized using chemical precipitation, a simple and efficient method, that allows precise control over composition and particle size. The precipitation occurs through the reaction between a magnesium ion source (such as magnesium nitrate, magnesium sulphate, or magnesium chloride) and a phosphate ion source (such as phosphoric acid, ammonium hydrogen phosphate, or sodium phosphate) under carefully controlled *p*H and temperature conditions [22–24].

Electrospinning is a widely used technique for producing polymer nanofibers that mimic the architecture of the extracellular matrix. Its basic principle relies on the application of a high electric field to a polymer solution, generating a fine jet that elongates and solidifies into continuous fibres [25,26]. Matrix-Assisted Pulsed Laser Evaporation (MAPLE) is a thin-film deposition technique that enables the controlled transfer of sensitive materials onto substrates through laser-induced evaporation of a frozen target, allowing precise surface functionalization without altering their chemical structure [27,28]. These methods enable fine control over scaffold morphology and bioactivity, making them suitable for tissue engineering applications.

MgP has attracted considerable attention in bone regeneration due to its high initial strength and ability to release bioactive ions that stimulate osteoblast proliferation and differentiation [29]. Specifically, MgP phases such as $Mg_3(PO_4)_2$ (farringtonite) and the thermally derived $Mg_2P_2O_7$ (magnesium pyrophosphate) exhibit suitable mechanical properties for bone tissue engineering applications. MgP-based scaffolds are reported to exhibit a compressive modulus of approximately 43 MPa and a compressive strength of approximately 19 MPa, while $Mg_2P_2O_7$ has been reported to reach compressive strength values in the range of approximately 10–50 MPa, depending on processing conditions [29]. For comparison, trabecular bone presents a compressive modulus in the range of 120–1100 MPa and compressive strength values between 0.1 and 16 MPa, depending on anatomical location and density [29]. These indicate that MgP-based materials exhibit compressive strength values within or slightly above the range of trabecular bone, while their elastic modulus remains lower than that of native bone. This makes them suitable for applications requiring moderate mechanical support, particularly in trabecular bone regeneration, where the scaffold is not required to sustain high mechanical loads. Furthermore, the presence of the $Mg_2P_2O_7$ phase contributes to improved structural stability and controlled degradation, which are essential for maintaining temporary support while enabling gradual replacement by newly formed bone tissue [22–24,29].

The $Mg_2P_2O_7$ phase is characterized by a relatively low solubility and enhanced structural stability in physiological environments, enabling a more controlled degradation behaviour and sustained ion release compared to $Mg_3(PO_4)_2$, which typically exhibits faster dissolution. This improved stability allows $Mg_2P_2O_7$ to maintain its structural integrity for a longer period, providing more consistent mechanical support during the early stages of bone healing. This balance between stability and resorption is essential for maintaining temporary mechanical support while allowing gradual replacement by newly formed bone tissue. In addition, $Mg_2P_2O_7$ contributes to the formation of stable crystalline phases and

may support osteogenic activity through its interaction with biological ions, promoting processes such as mineralization and osteoblast differentiation [22–24,29].

From a clinical perspective, these properties make $Mg_2P_2O_7$-containing systems particularly suitable for bone void fillers, bone cements, and the repair of trabecular bone defects, where controlled resorption, mechanical stability, and bioactivity are required. Moreover, its use as a stabilizing phase can improve the structural integrity of composite scaffolds while maintaining a degradation rate compatible with new bone formation, offering an advantage over more soluble magnesium phosphate phases.

A similar study [30] also explored the incorporation of nano-sized MgP (nMP) into electrospun scaffolds composed of polycaprolactone (PCL), hyperbranched polyglycerol (HPG), and nano-hydroxyapatite (nHA). The study demonstrated that these composite scaffolds exhibit improved hydrophilicity, enhanced degradability, increased mineralization, and superior mechanical properties. Another study [31] reported the development of a 3D-printed $Mg_3(PO_4)_2$/PCL scaffold designed for maxillofacial bone defect repair. In vitro results demonstrated that PCL scaffolds containing 20% $Mg_3(PO_4)_2$ significantly enhance osteogenic differentiation, while in vivo experiments using rat tibial defect models confirmed their strong bone-regenerative capacity, as well as their superior therapeutic efficacy compared to pure PCL scaffolds.

In this study, the objectives were: (i) the synthesis of MgP powders, (ii) the fabrication of electrospun PCL fibres, and (iii) the deposition of the phosphate phases as a thin coating on the surface of the electrospun fibres. The current focus in the field has been predominantly on the incorporation of MgP particles within polymer matrices, which can limit direct interaction with the biological environment and delay ion release. In this context, surface functionalization strategies remain relatively underexplored. Depositing the bioactive powders onto the fibres surface enhances interaction with the damaged tissue and enables faster and more efficient ion release, overcoming the slow degradation rate of PCL (~2 years) [32,33], which would otherwise delay the release of magnesium and phosphate ions if the powders were embedded within the polymer matrix. In addition, the use of the MAPLE technique to deposit phosphate phases as a uniform and controllable coating on the surface of electrospun PCL fibres represents a key innovative aspect, providing precise and reproducible surface functionalization that strengthens the interface between the scaffold and the biological environment. This controlled deposition significantly improves ion exchange dynamics and promotes more effective biological interactions, ultimately enhancing the regenerative performance. This approach results in multifunctional scaffolds combining mechanical support with enhanced bioactivity, suitable for bone tissue engineering applications.

2. Materials and Methods

2.1. Materials

The following reagents were used for the synthesis of MgP powders and for polymeric scaffolds fabrication: magnesium nitrate hexahydrate ($Mg(NO_3)_2{\cdot}6H_2O$, ≥99%, Sigma-Aldrich, Darmstadt, Germany), ammonium phosphate dibasic ($(NH_4)_2HPO_4$, ≥99%, Sigma-Aldrich), lithium acetate dihydrate ($CH_3COOLi{\cdot}2H_2O$, ≥99%, Sigma-Aldrich), zinc acetate dihydrate ($(CH_3COO)_2Zn{\cdot}2H_2O$, ≥99%, Sigma-Aldrich), ammonium hydroxide (NH_4OH, 25% solution, Sigma-Aldrich), and distilled water. For electrospun fibre preparation, poly(ε-caprolactone) (PCL, average molecular weight 80,000 g/mol, Sigma-Aldrich) was used as the polymer, while chloroform (CF, ≥99.8%, Sigma-Aldrich) and N,N-dimethylformamide (DMF, ≥99.8%, Sigma-Aldrich) served as solvents. Nutrient Broth No. 2, Sabouraud Broth, sodium chloride (NaCl), methanol (CH_3OH, 99.9%), crystal violet ($C_{25}N_3H_{30}Cl$), and acetic acid (CH_3COOH, ≥99%) from Sigma-Aldrich

were used for antimicrobial assays. Standard strains were provided from the Microorganism Collection of the Microbiology Laboratory of the Department of Oxide and Nanomaterials Science and Engineering, Faculty of Chemical Engineering and Biotechnology.

2.2. Synthesis Methods

2.2.1. Powders Preparation

Three types of MgP powders were synthesized using chemical precipitation method: MP (undoped), MLP (lithium-doped) and MZP (zinc-doped), as can be seen in Table 1. The dopant concentrations were selected within biologically relevant ranges, with lithium maintained around 10% to avoid potential cytotoxic effects, and zinc within the 1–5% range to enhance cellular proliferation while preserving cytocompatibility.

Table 1. Dopant concentration of MgP powders.

Sample Code	Dopant Concentration (%)	Chemical Formula
MP	0.00	$Mg_2P_2O_7$
MLP	12.5	$Mg_{1.75}Li_{0.25}P_2O_7$
MZP	5.0	$Mg_{1.90}Zn_{0.10}P_2O_7$

Briefly, the calculated amounts of $Mg(NO_3)_2 \cdot 6H_2O$ and the corresponding dopant salt ($CH_3COOLi \cdot 2H_2O$ and $(CH_3COO)_2Zn \cdot 2H_2O$) were dissolved in distilled water and stirred magnetically at room temperature to obtain the first solution. Separately, $(NH_4)_2HPO_4$ was dissolved in distilled water to prepare the second solution. The first solution was added dropwise to the second solution under continuous stirring, followed by the gradual addition of NH_4OH to adjust the pH to 9, resulting in the formation of a milky white precipitate. The precipitate was collected by filtration, washed multiple times with distilled water to remove residual ions, and dried at 100 °C for 24 h. Finally, the powders were calcined at 800 °C for 2 h to obtain the final powders. According to the literature [8], at elevated temperatures, crystalline peaks start to appear, and at around 800 °C, well-defined crystalline peaks of MgP-based phases are observed, which have been attributed to the formation of magnesium pyrophosphate ($Mg_2P_2O_7$).

2.2.2. Fibres Fabrication

The PCL solution was prepared by dissolving a fixed amount of PCL polymer in a mixture of CF and DMF solvents at a 3:1 ratio to obtain a 10 wt% solution. The solution was stirred at room temperature using a magnetic stirrer for 24 h to ensure complete dissolution. For electrospinning, 5 mL of the PCL solution was loaded into a 10 mL syringe equipped with a 22G metallic needle (0.7 mm outside diameter, 0.4 mm inside diameter) and mounted on a syringe pump to control the flow rate. Fibres were collected on aluminium foil or glass slides placed on the collector plate. The same electrospinning process parameters were continued for each solution, such as solution flow rate at 0.5 mL/h, electric field voltage of 15 kV, and needle-to-collector distance of 15 cm.

2.2.3. Coated Fibres Manufacturing

For the deposition of MgP powders (MP, MLP, and MZP) onto PCL fibres, the MAPLE technique was employed, resulting in three composite fibre types: PCL-MP, PCL-MLP, and PCL-MZP (Table 2). Prior to deposition, all powders were calcined at 800 °C to remove impurities and volatile components, as well as to improve their thermal and mechanical stability. The calcined powders were then ground and sieved through a 75 μm mesh to obtain a fine, uniform particle size distribution.

Table 2. Composition of MAPLE-coated PCL fibres.

Sample Code	Polymer	Powder Deposition
PCL-MP	PCL	Magnesium Phosphate (MP)
PCL-MLP		Magnesium Lithium Phosphate (MLP)
PCL-MZP		Magnesium Zinc Phosphate (MZP)

For MAPLE target preparation, each powder was dispersed in dimethyl sulfoxide (DMSO, ≥99.7%, Sigma-Aldrich) at a concentration of 10 g/L by dissolving 0.05 g of powder in 5 mL of solvent. The resulting suspensions were then frozen by immersion in liquid nitrogen, forming solid targets. Laser irradiation of the frozen targets was performed using a KrF* excimer laser source from Coherent (Göttingen, Germany, CompexPro 205, λ = 248 nm, $\tau_{FWHM} \sim 25$ ns) operated at 20 Hz and a fluence of 300 mJ/cm^2. The laser-induced solvent evaporation promoted the transfer of material molecules towards the substrate, positioned 5 cm from the target inside a vacuum chamber maintained at 2×10^{-4} mbar. Both the target and substrate were rotated to ensure uniform and reproducible coating of the fibres. The main fabrication steps are displayed in Figure 1.

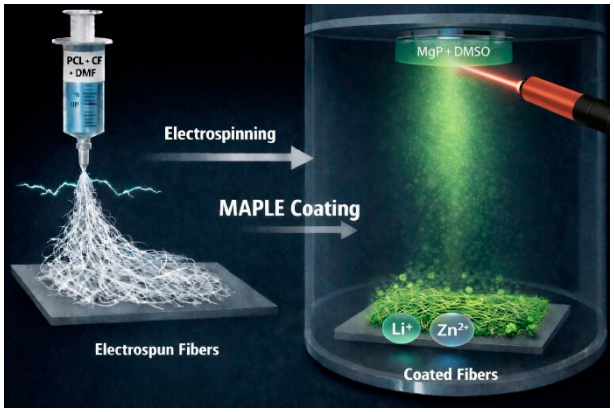


Figure 1. Schematic representation of the fabrication process for phosphate-coated PCL fibres. This was obtained after multiple iterative refinements using ChatGPT (OpenAI, GPT-5.3-mini, San Francisco, CA, USA), guided by the authors to accurately reflect the experimental setup.

2.3. Characterization Methods

2.3.1. Thermal Analysis

Thermal analysis was carried out using a Netzsch STA 449 F3 Jupiter (Netzsch, Germany) equipment. Measurements were performed from room temperature up to 900 °C, with a heating rate of 10 °C/min under oxidizing atmosphere, in order to determine the thermal stability and composition of the samples.

2.3.2. Scanning Electron Microscopy (SEM) Coupled with Energy-Dispersive X-Ray Spectroscopy (EDX)

The morphology and particle size were analysed by SEM using a FEI Quanta Inspect F50 (FEI, Hillsboro, OR, USA), operated at 30 kV, in secondary electron mode. For elemental composition, EDX was employed, and samples were gold-coated by DC sputtering for 60 s prior to observation.

2.3.3. Attenuated Total Reflectance—Fourier Transform Infrared Spectroscopy (ATR-FTIR)

The molecular structure of the samples was studied by ATR-FTIR using a Nicolet iS50 spectrometer (Thermo Fisher Scientific, Waltham, MA, USA). Spectra were collected in the 400–4000 cm^{-1} range, with 4 cm^{-1} resolution and 32 scans per sample.

2.3.4. X-Ray Diffraction (XRD)

Phase identification and crystallinity were investigated by XRD using a Shimadzu XRD-6000 diffractometer (Shimadzu, Kyoto, Japan). Measurements were performed with CuKα radiation (λ = 0.154 nm) over the 2θ range of 20–80°, with a scanning speed of 2°/min and a step size of 0.02°.

2.3.5. X-Ray Photoelectron Spectroscopy (XPS)

Surface chemical composition was examined by XPS with a Thermo Scientific K-Alpha spectrometer (Thermo Fisher Scientific, Waltham, MA, USA). Analyses were performed using a monochromatic AlKα source (1486.6 eV) under a base pressure of 2×10^{-9} mbar. The pass energy for the survey spectra was 200 eV, while that for the high-resolution spectra recording was 20 eV.

2.3.6. Antimicrobial Activity

Firstly, the developed powders and fibres were sterilized for 30 min of UV radiation on each part. The antimicrobial properties of the developed materials were evaluated using methods described in previous studies [34,35] and according to the Clinical Laboratory Standards Institute guidelines [36]. Standardized microbial suspensions (1.5×10^8 CFU/mL) were prepared in phosphate-buffered saline (PBS) from 24 h cultures of *Enterococcus faecalis* ATCC 29212, *Staphylococcus aureus* ATCC 25923, *Staphylococcus epidermidis* ATCC 1228, *Escherichia coli* ATCC 25922, *Pseudomonas aeruginosa* ATCC 27853, *Salmonella typhimurium* ATCC 14028, and *Candida albicans* ATCC 10231.

The antimicrobial profiles of developed powders were quantitatively evaluated using the minimum inhibitory concentration (MIC) assay [34]. In 96-well plates, serial two-fold microdilutions from 10 μg/μL to 0.08 μg/μL for each sample were performed in 150 μL of specific broth for the tested strains. The wells were seeded with 15 μL of the standard inoculum, and the plates were incubated at 37 °C for 24 h. Due to the deposition of precipitate (powders) at the bottom of the wells, visual observations were realized, and 100 μL from each well were transferred to another plate for performing spectrophotometric measurements at 620 nm using the SpectraMax i3 Multi-Mode Microplate Reader (Molecular Devices, San Jose, CA, USA). Furthermore, the biofilm development on the inert substratum was determined using the same plates that had been incubated for 24 h. After MIC measurements were performed, the media from the plates was removed, the walls were washed three times with PBS, and the bacterial cells adhered to the walls were fixed with methanol (5 min) and tinted with 1% crystal violet (15 min). The dyed biofilm was resuspended with 33% acetic acid, and the absorbance was measured at 492 nm [34].

The antibacterial properties of developed fibres were qualitatively evaluated using an adapted diffusion method [35]. Petri dishes were inoculated with standardized suspensions of *E. coli* ATCC 25922, after which the samples were positioned with the treated surface in direct contact with the inoculated Nutrient agar medium. After 24 h of incubation, the diameters of growth inhibition zones were measured using ImageJ software (version 1.8.0, National Institutes of Health, Madison, WI, USA).

2.3.7. Simulated Body Fluid (SBF) Immersion Test

Bioactivity was assessed by immersing the samples in simulated body fluid (SBF), prepared according to Kokubo's protocol [37]. The specimens were kept at 37 °C for 28 days in 1.7 mL SBF, and the degradation behaviour of the PCL fibres was evaluated.

2.3.8. MTT Assay for Cell Viability

Cell biocompatibility was investigated using human fetal osteoblasts (hFOB 1.19, ATCC, Manassas, VA, USA). Cells were cultured in a 1:1 mixture of Ham's F12 and Dulbecco's Modified Eagle's Medium (DMEM), supplemented with 10% fetal bovine serum (FBS) and 1% penicillin/streptomycin (Thermo Fisher Scientific, USA). The cultures were maintained in a humidified incubator at 37 °C and 5% CO_2. Given that the doubling time of hFOB cells exceeds 24 h, the cells were seeded onto the samples and allowed to grow for 48 h prior to the viability assessment [38]. Cell metabolic activity was quantified using the MTT assay, and additional morphological characterization was performed by optical and fluorescence microscopy. The analyses were performed on five different types of surfaces: a glass substrate used as the control, pure PCL fibres used as the reference, and the composite fibres (PCL-MP, PCL-MLP, PCL-MZP).

2.3.9. Cell Morphology

Cell morphology was evaluated by both transmission and fluorescence microscopy. First, the cells were imaged using a transmission microscope at 48 h after seeding and images were recorded using a 10× objective. Finally, the cell nucleus and cytoskeleton were stained according to the following protocol. After 48 h, the cells were fixed using a 3% paraformaldehyde solution, permeabilized with 0.1% Triton X-100; actin filaments were stained with FITC-phalloidin (Thermo Fisher Scientific, USA) and nuclei with Hoechst 33342 (Thermo Fisher Scientific, USA). Slides were mounted using FluorSaveTM and imaged using an Olympus BX-51 epifluorescence microscope (Tokyo, Japan) equipped with a 40× objective and DAPI/Hoechst and GFP/FITC filters.

3. Results and Discussion

3.1. Powders Characterization

3.1.1. Thermal Analysis

Thermal analysis of undoped precipitate was performed up to 900 °C, as shown in Figure 2 by TGA, DTG, and DSC curves. The TGA curve indicates a total mass loss of ~34%, mainly due to dehydration followed by decomposition and phase reorganization. The DTG profile reveals a pronounced peak around 100 °C, corresponding to rapid water loss, while subsequent changes are attributed to the conversion of metastable or amorphous phases into more stable compounds.

DSC analysis shows a broad endothermic peak near 150 °C, associated with dehydration, and a clear exothermic peak between 700 and 800 °C, suggesting structural reorganization and crystallization, likely related to the formation of magnesium pyrophosphate ($Mg_2P_2O_7$), as reported in the literature [29]. This exothermic event reflects the condensation of phosphate groups ($PO_4^{3-} \rightarrow P_2O_7^{4}$) into a thermodynamically more stable crystalline phase.

This newly formed phase results from the reorganization of phosphate tetrahedra into P–O–P bridging units, which reduces the overall free energy of the system and promotes long-range structural ordering, leading to a more compact and energetically favourable structure. Owing to its controlled solubility, gradual ion release, and intrinsic biocompatibility, this stable phase is considered suitable for biomedical applications, particularly in bone repair materials where a balance between structural integrity and resorption is required [12,39].

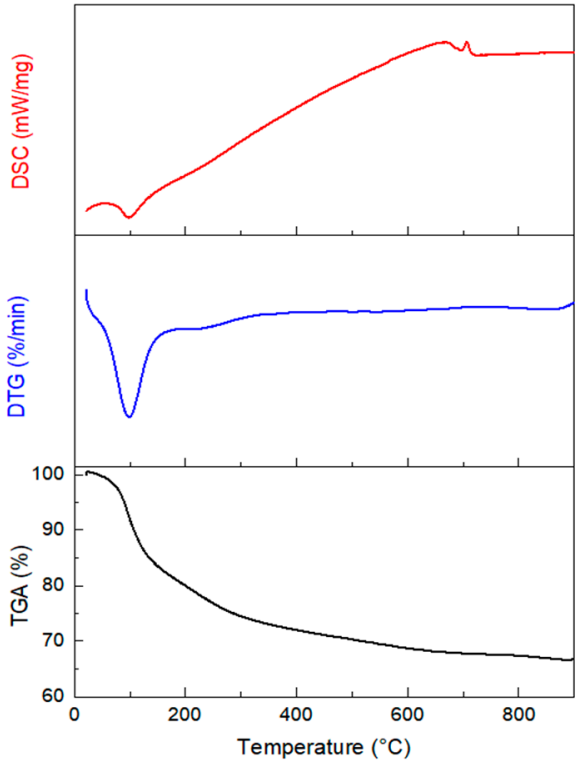


Figure 2. Thermal analysis of the MP precipitate.

3.1.2. Scanning Electron Microscopy (SEM)

The SEM images in Figure S1 show the powders, MP (A,B), MLP (C,D), and MZP (E,F), at 100 µm scale for a broader surface overview and 10 µm for detailed morphological observations, prior to thermal calcination. MP exhibits irregular aggregates of varying sizes, with both sharp and rounded edges. Image (A) shows relatively uniform dispersion, whereas image (B) reveals more pronounced agglomerates and surface pores, which could affect the material interaction with other substances. For the doped samples, larger and denser aggregates are observed. Image (C) shows well-defined, more homogeneous entities for MLP; in image (D), the aggregates are smoother compared to MP, with similar shapes and sizes, suggesting increased material homogeneity when integrating lithium. MZP displays even more distinct shapes and dispersion of aggregates, reflecting improved uniformity after zinc doping. In image (E), aggregates are relatively uniform, while in (F) they appear coarser, more compact, and more square-shaped, with less pronounced pores, indicating densification of the material due to zinc incorporation.

Figure 3 shows the morphological changes induced by thermal calcination at 800 °C. In image (A), MP aggregates are more densely packed and larger compared to the uncalcined powder. Image (B) shows increased porosity, with large cavities; the particles appear irregular and sintered, with voids formed due to the removal of certain phases during calcination. MLP displays flat surfaces, with well-defined edges. The aggregates are larger, more compact, and more homogeneous than in the undoped or zinc-doped powders. Porosity is significantly reduced due to particle fusion, and the distribution is more uniform compared to pre-calcined MLP, potentially improving the mechanical properties. In the case of MZP, images (E,F) reveal smoother surfaces, with more uniformly distributed, smaller pores. The particles are denser and more homogeneous, showing a stronger tendency to form compact aggregates.

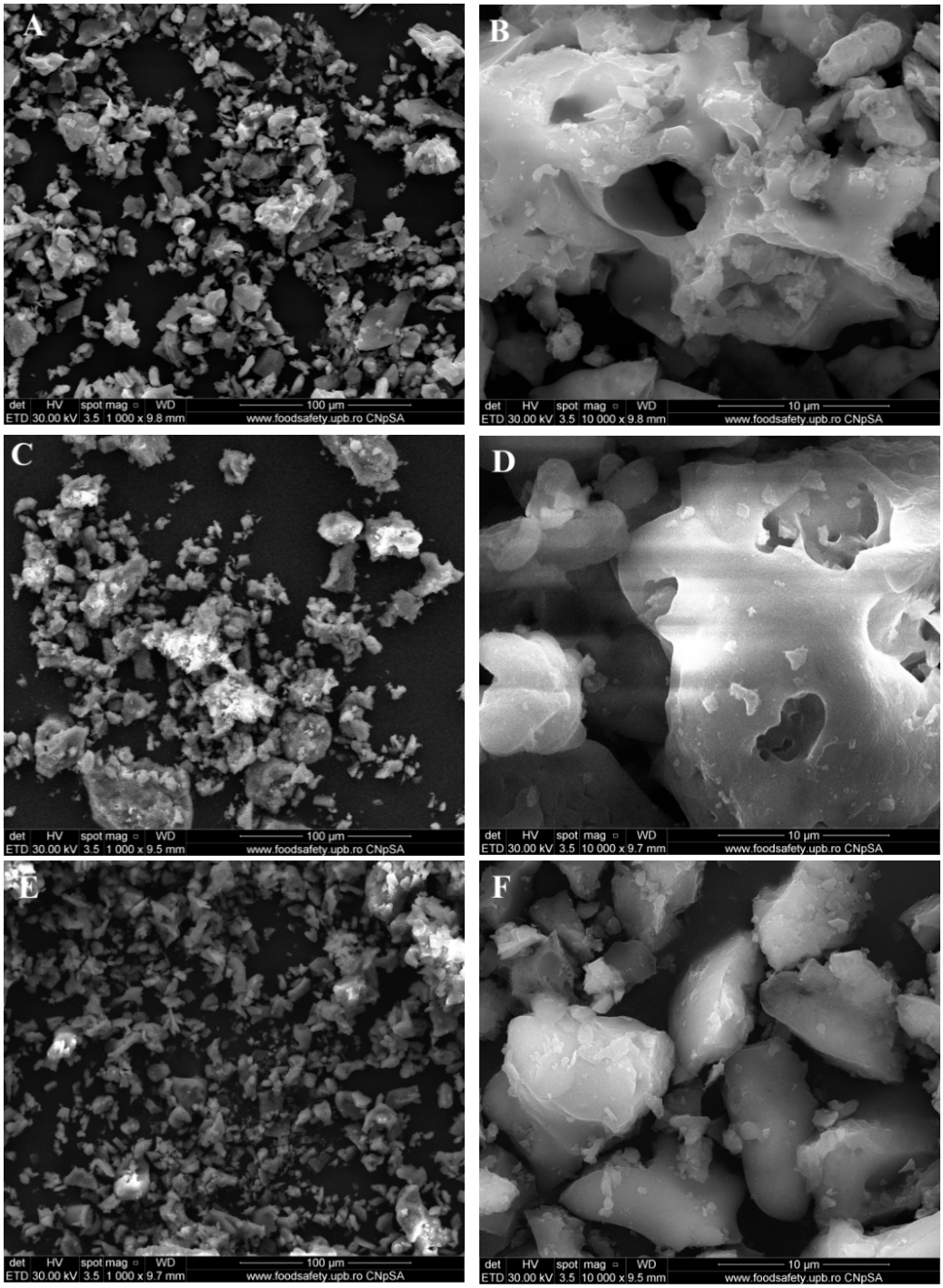


Figure 3. SEM images of: (**A**,**B**) MP, (**C**,**D**) MLP, and (**E**,**F**) MZP powders after thermal treatment.

3.1.3. Energy-Dispersive X-Ray Spectroscopy (EDX) and Attenuated Total Reflectance—Fourier Transform Infrared Spectroscopy (ATR-FTIR)

Figure 4A,B shows that the powders are mainly composed of magnesium (Mg), phosphorus (P), and oxygen (O), with similar concentrations across all three compositions, both before and after calcination. Minor zinc (Zn) signals appear only in the case of MZP, consistent with its doping, while lithium (Li) could not be detected in MLP due to the inability of EDX to identify very light elements. In the uncalcined samples (Figure 4A), small nitrogen (N) peaks originate from the magnesium nitrate precursor ($Mg(NO_3)_2 \cdot 6H_2O$), whereas carbon (C) and aluminium (Al) signals arise from the carbon tape and the aluminium support, respectively. Gold (Au) is present due to the sputter-coating required

for these non-conductive powders. After calcination (Figure 4B), a reduction in organic residues and impurity-related signals is observed, indicating purification and stabilization of the material.

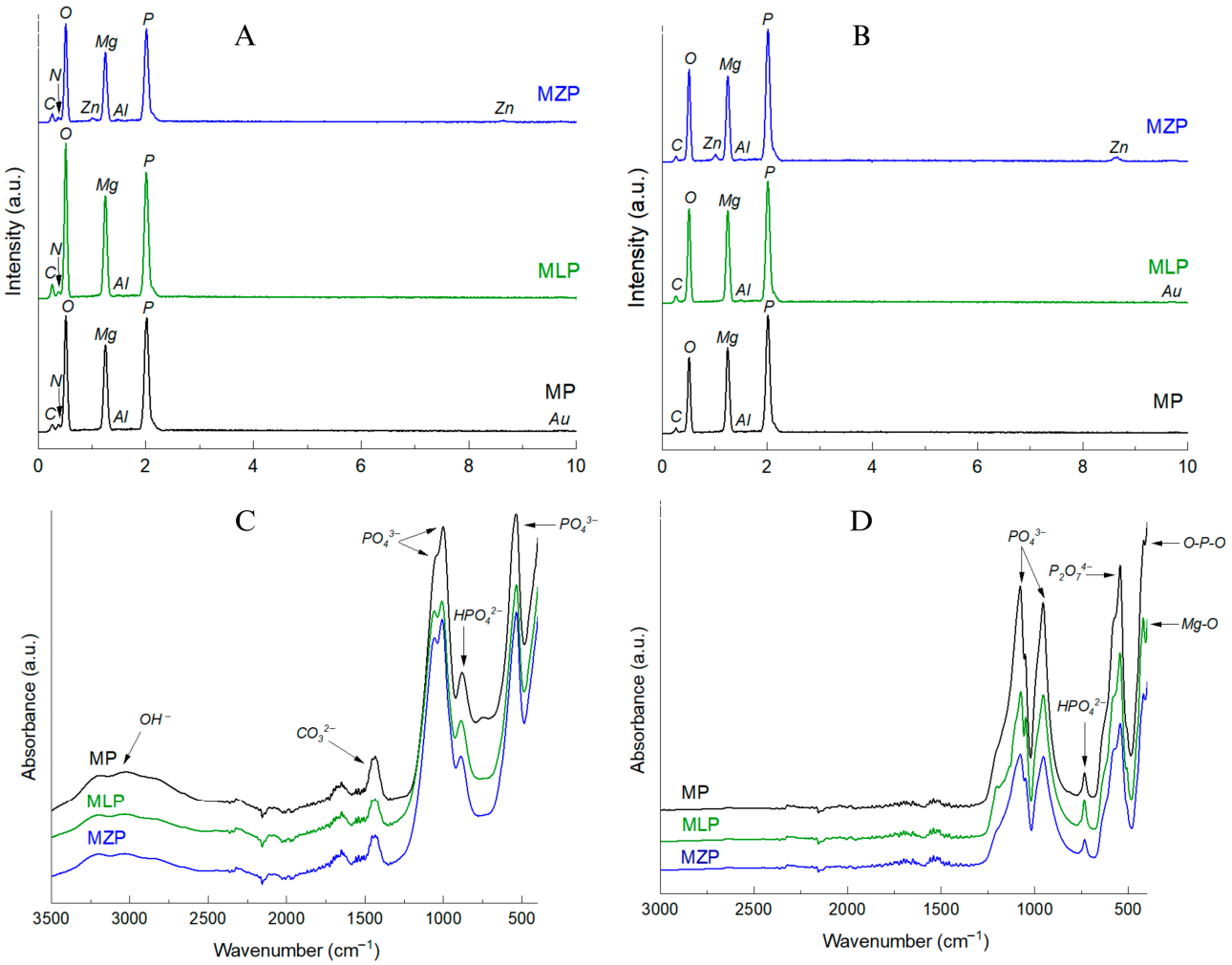


Figure 4. EDX spectra of: (**A**) uncalcined and (**B**) calcined powders and ATR-FTIR spectra of: (**C**) uncalcined and (**D**) calcined powders.

The ATR-FTIR spectra shown in Figure 4C present characteristic peaks of the powders before calcination. Vibrational bands corresponding to hydroxyl (OH^-) groups are observed in the 3500–3200 cm^{-1} range, indicating the possible presence of residual water. Carbonate (CO_3^{2-}) groups appear in the 1300–1600 cm^{-1} range, likely due to CO_2 absorption during or after synthesis, or from precursor contamination. Phosphate (PO_4^{3-}) vibrations are visible at 560–600 cm^{-1}, 960 cm^{-1}, and 1020–1120 cm^{-1}; the more intense bands in MP suggest a better-organized phosphate structure compared to MLP or MZP, indicating that doping may induce lattice distortions, broadening the bands and reducing peak intensities [40]. Additionally, as magnesium content increases, the vibrational band at 875 cm^{-1}, associated with hydrogen phosphate (HPO_4^{2-}) groups, decreases in intensity, reflecting stabilization of the phosphate groups in the material [40].

The ATR-FTIR spectra obtained after calcination (Figure 4D) show vibrational bands characteristic of phosphate and pyrophosphate structures. The intense band in the 1020–1120 cm^{-1} region is assigned to the asymmetric stretching of phosphate (PO_4^{3-}) groups, while the well-defined peak around 960 cm^{-1} corresponds to symmetric stretching of the same group. The 875 cm^{-1} band observed for the uncalcined samples and associated with hydrogen phosphate (HPO_4^{2-}) decreases significantly after calcination,

indicating nearly complete transformation into more stable structures. The weak or absent carbonate (CO_3^{2-}) and hydroxyl (OH^-) bands further confirm structural purification of the material [41]. Notably, a new peak around 740 cm^{-1} appears, attributed to P–O–P stretching, marking the formation of pyrophosphate ($P_2O_7^{4-}$) groups [41,42]. This transition is accompanied by O–P–O bending vibrations in the 600–500 cm^{-1} region, characteristic of a well-organized phosphate network, as well as possible Mg–O vibrational bands below 500 cm^{-1} [42,43].

3.1.4. X-Ray Diffraction (XRD)

Figure 5A shows the XRD patterns of the powders prior to thermal treatment. Broad diffraction bands in the range 2θ = 20–35° indicate an amorphous or poorly crystalline structure. Compared with MP, doping with zinc (MZP) or lithium (MLP) slightly shifts and narrows the diffraction peaks, reflecting modifications in the material structural order. In particular, MZP exhibits sharper and better-defined peaks, suggesting increased crystallinity, consistent with literature reports that zinc doping promotes the formation of more ordered crystalline phases [43]. In contrast, lithium doping appears to inhibit crystallization, likely due to the larger ionic radius (Li^+—0.76 Å, Mg^{2+}—0.72 Å) and monovalent charge, which locally perturbs the crystal lattice and increases structural disorder [41].

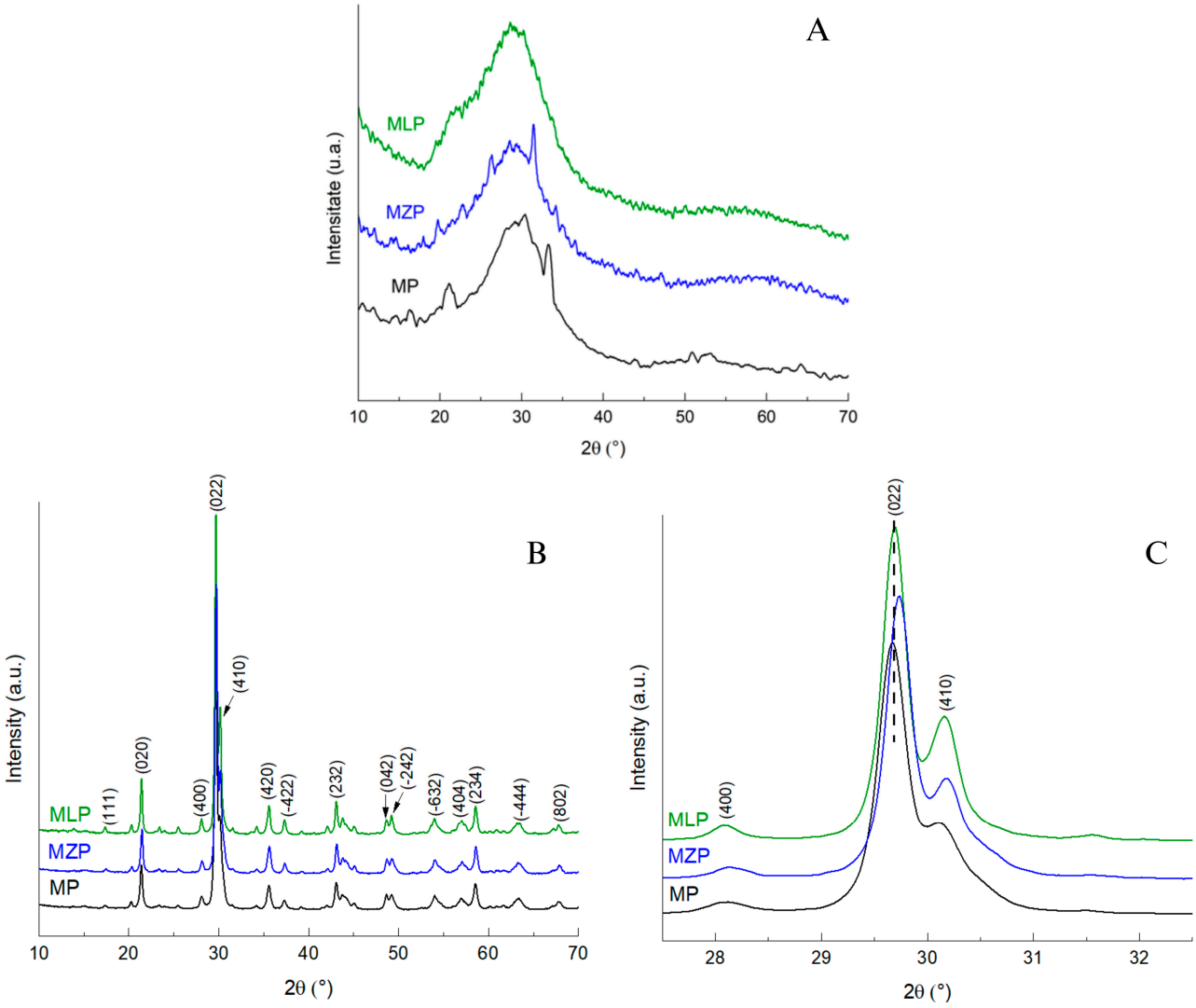


Figure 5. XRD patterns of: (**A**) uncalcined and (**B**,**C**) calcined powders.

Figure 5B shows the XRD patterns of the powders after thermal treatment. Compared to the previously amorphous state, well-defined and intense diffraction peaks appear, corresponding to $Mg_2P_2O_7$ (ICDD 00-075-1055) [39], indicating the formation of a more stable crystalline structure. All three samples exhibit similar diffraction maxima, suggesting the same basic crystallographic phase, with minor intensity variations due to zinc and lithium doping.

In Figure 5C, where a graphical representation of the previous plot over a narrower angle range is displayed, a slight shift of the diffraction peak at $2\theta \approx 30°$, plane (022), is observed, particularly for MZP, indicating a slight lattice expansion induced by doping. According to the literature data [44], Mg^{2+} in sixfold coordination has an ionic radius of 0.72 Å, whereas Zn^{2+} and Li^{+} have radii of 0.74 Å (+2.7%) and 0.76 Å (+5.5%), respectively. Although these differences are small, they can affect how dopant ions are incorporated into the lattice. Zn^{2+}, with a slightly larger ionic radius than Mg^{2+}, can substitute directly into magnesium sites, leading to a slight expansion of the crystal lattice, consistent with the observed peak shift toward lower 2θ angles in the XRD patterns [43,44]. In contrast, monovalent Li^{+}, with a larger radius, integrates less readily into magnesium sites, causing greater local lattice rearrangements and slightly distorted domains without significantly altering peak positions [19].

3.1.5. X-Ray Photoelectron Spectroscopy (XPS)

The presence of lithium in the material was confirmed by XPS analysis of the calcined powders, as shown in Figure 6. For the MLP sample, lithium incorporation causes slight shifts in the binding energies of high-resolution spectra of magnesium (Mg 1s), phosphorus (P 2p), and oxygen (O 1s), indicating changes in the local chemical environment. These shifts are consistent with the larger ionic radius of Li^{+} (0.76 Å) compared with Mg^{2+} (0.72 Å) [44], which generates local lattice distortions and perturbs the surrounding bonding environment. This behaviour agrees with the XRD results, where lithium produces broader diffraction halo and negligible peak shifts, reflecting attenuated structural order. In contrast, Zn^{2+}, with an ionic radius of 0.74 Å [44], close to that of Mg^{2+}, can be readily incorporated into magnesium sites. This substitution may induce a slight expansion of the crystal lattice, as suggested by subtle shifts in the diffraction peaks toward lower 2θ angles in the XRD patterns, along with minor changes in binding energies observed by XPS [43]. The lower designed concentration for lithium also contributes to its weaker XPS analysis, although the observed shifts still confirm its incorporation into the lattice [19].

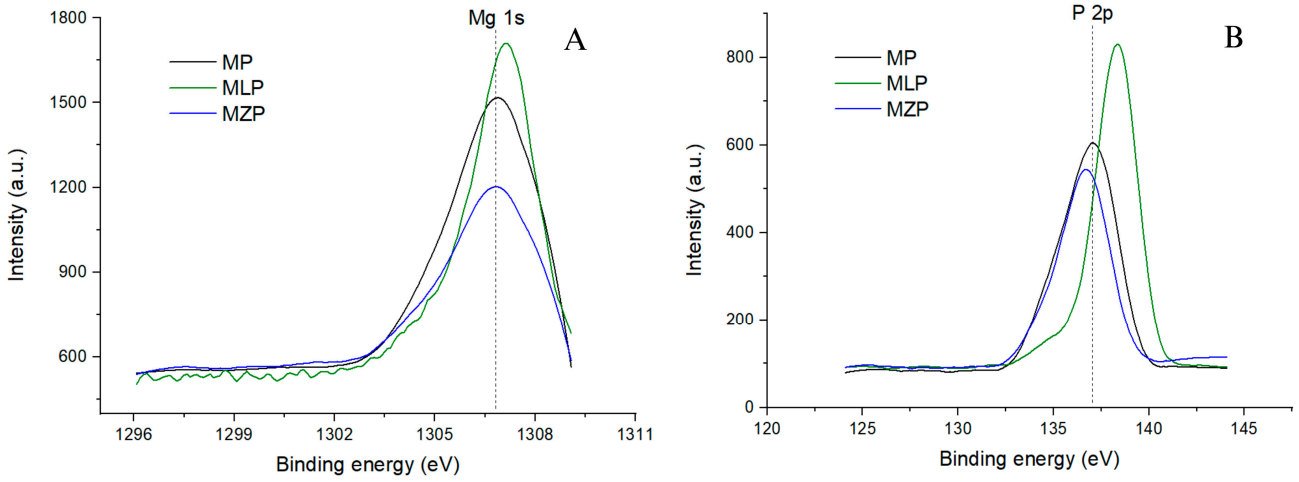


Figure 6. *Cont.*

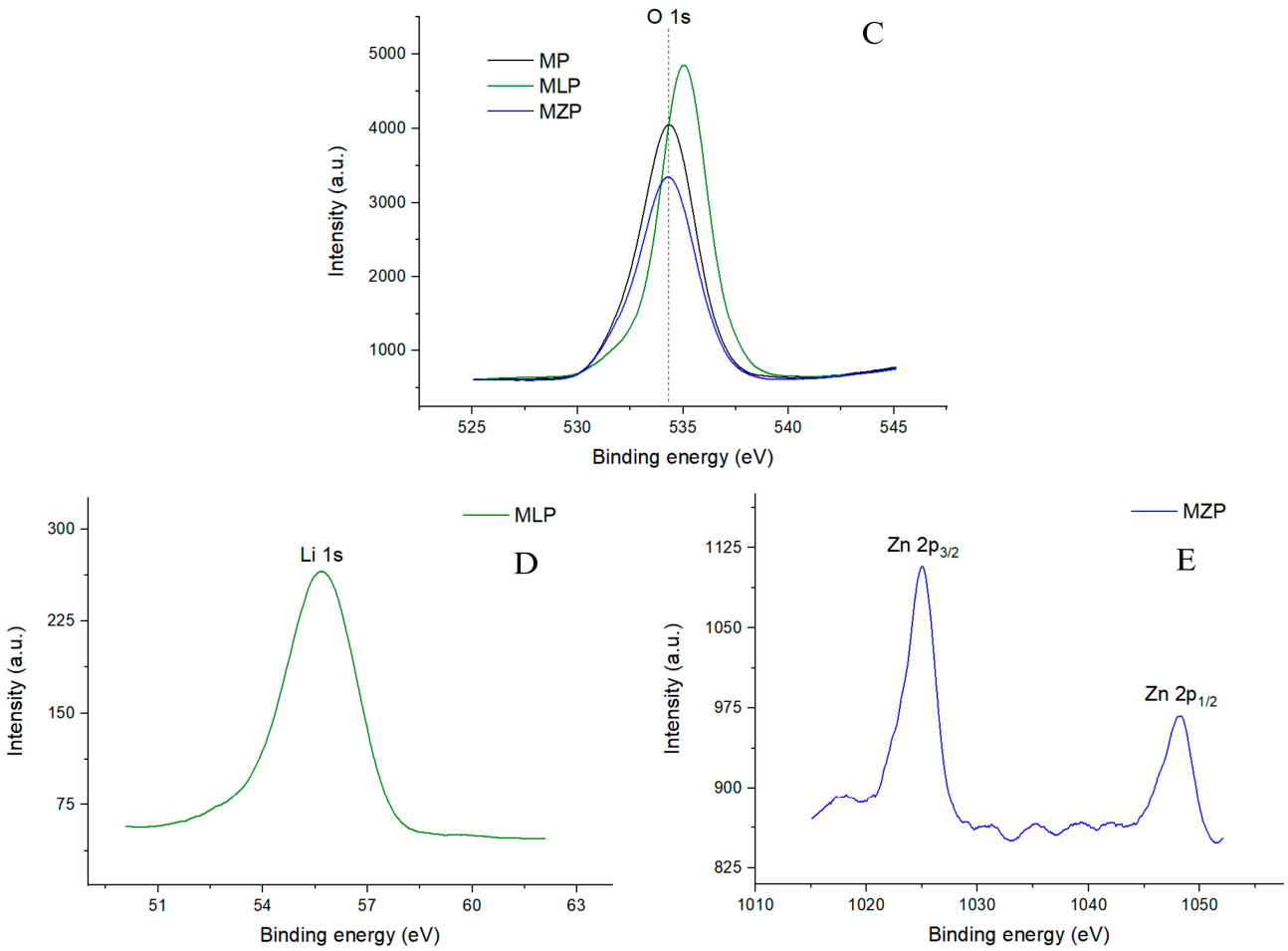


Figure 6. XPS spectra of the calcined powders: (**A**) magnesium, (**B**) phosphorus, (**C**) oxygen, (**D**) lithium detected only in the MLP sample, and (**E**) zinc detected only in the MZP sample.

3.1.6. Antimicrobial Assays

Firstly, the antimicrobial profiles of MgP powders were quantified by determining the MIC values (Figure 7), which are represented by the lowest concentration that inhibited microbial development.

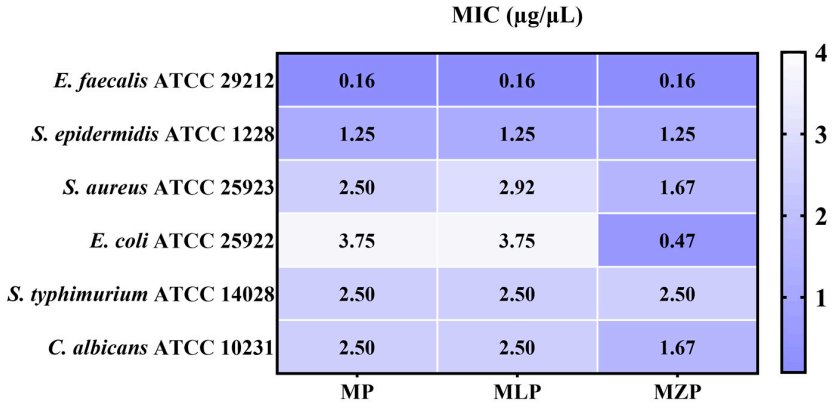


Figure 7. Heat map of MIC values. Data results marked in blue indicate the significantly lowest MIC values and highest sensitivity of strains. The scale bar shows the variations in the sensitivity of tested strains from the highest (blue) to the lowest (white).

The data shown in Figure 7 highlights the significant inhibitory effects of MgP powders against Gram-positive and Gram-negative bacteria. *E. faecalis* and *S. epidermidis* were the most sensitive bacteria with MIC values that range from 1.25 to 0.16 μg/μL. Moreover, the

addition of zinc enhances the sensitivity of tested strains, especially in the case of *E. coli* and *C. albicans*. The notable inhibitory effects of MZP powder are highlighted in the smallest MIC values, which range from 2.50 to 0.16 µg/µL.

Secondly, the influence of MgP powders on the adherence of the pathogenic strains to the inert substratum was performed and is represented by the minimal biofilm eradication concentration (MBEC) values (Figure 8).

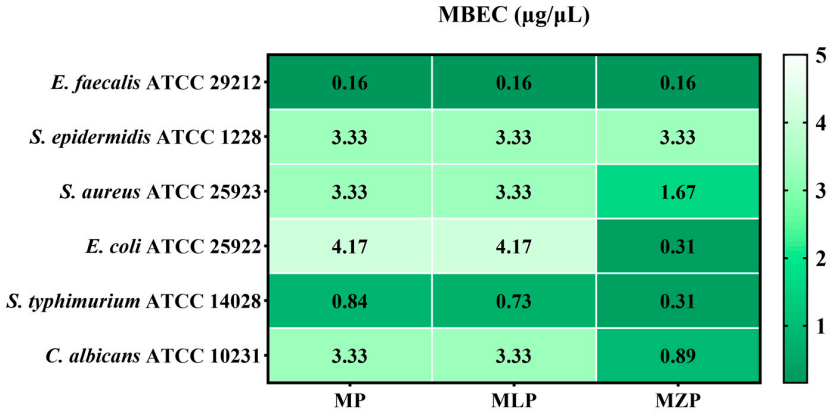


Figure 8. Heat map of MBEC values. Data results marked in forest green indicate the significantly lowest MBEC values and highest sensitivity of strains. The scale bar shows the variations in the sensitivity of tested strains from the highest (forest green) to the lowest (white).

The antibiofilm results presented in Figure 8 confirm the MIC data (Figure 7) and highlight the sensitivity of the strains to zinc ions. *E. faecalis* was the most sensitive strain in the presence of all MgP powders, with 0.16 µg/µL MBEC values. However, *S. epidermidis* adherence was less inhibited by MgP samples, which significantly inhibited the adhesion of *S. typhimurium*. Otherwise, the MLP powder does not exert notably inhibitory effects compared to the undoped powder, which indicates that a higher concentration is necessary. According to other studies [15,19], Li^+ concentrations above 5–10% have noticeable effects on microbial growth, although such levels may reduce the material biocompatibility. In contrast, the Zn^{2+} ions from MZP powder strongly inhibited the adhesion of tested pathogenic strains, with MBEC values that range from 3.33 to 0.16 µg/µL. These results are supported by several studies [16–18,45], which attribute a direct antimicrobial mechanism to zinc through oxidative stress generation, bacterial membrane disruption, and interference with microbial enzymatic systems. Additionally, zinc promotes tissue healing, indirectly preventing infections.

3.2. Coated Fibres Characterization

MgP-based materials are known for their bioactivity, biodegradability, and ability to support bone regeneration, as demonstrated in many studies [8–11,29], where Mg-containing phosphate scaffolds were shown to promote osteogenesis while providing adequate mechanical support. In this context, the developed PCL–MgP composites are particularly suitable for trabecular bone defects, where moderate mechanical strength is required and rapid tissue ingrowth is essential. The presence of PCL plays a key role, as its relatively slow degradation rate allows the scaffold to maintain structural integrity over an extended period, providing sustained mechanical support during the early stages of healing. At the same time, due to their porous fibrous structure and controlled release of bioactive ions (Mg^{2+}, PO_4^{3-}, and dopant ions such as Li^+ and Zn^{2+}), these materials can support cell adhesion, proliferation, and differentiation, while gradually degrading and being replaced by newly formed bone. Such composites may be used for filling non-load-bearing bone defects, in maxillofacial bone regeneration, as bone void fillers following trauma or surgical

interventions, or as bioactive coatings for implants to enhance osteointegration. Therefore, they represent a promising alternative to autografts or conventional synthetic bone substitutes, with the advantage of eliminating donor site morbidity while providing a resorbable and bioactive scaffold.

3.2.1. Scanning Electron Microscopy (SEM) Coupled with Energy-Dispersive X-Ray Spectroscopy (EDX) and Attenuated Total Reflectance—Fourier Transform Infrared Spectroscopy (ATR-FTIR)

The SEM images shown in Figure 9 illustrate fibres obtained from pure PCL uncoated and coated with MP (PCL-MP), MZP (PCL-MZP), and MLP (PCL-MLP), at scales of 100 μm and 10 μm, deposited on an aluminium substrate. In images (A,B), continuous, fine, and uniformly distributed fibres can be observed, without visible discontinuities. Their surface appears smooth and homogeneous, free of major defects, with fibre diameters ranging between 150 and 800 nm. In images (C,D), the fibres remain continuous and well distributed across the surface; however, attached MP particles can be observed. These phosphate clusters, of variable dimensions, increase the surface roughness of the fibres and may affect pore distribution. Fiber diameters also vary, ranging from 100 nm up to 3 μm, with thicker regions influenced strongly by the electrospinning process parameters. Images (E,F) highlight the presence of particle aggregates, appearing brighter in contrast, attached to the fibres. These accumulations indicate a non-uniform distribution of MLP, with voids occurring in areas where larger particles are present. The fibres also exhibit variability in shape and size, with diameters ranging from 130 nm to 2 μm. Because the phosphate coating obtained by MAPLE forms a very thin surface layer, it cannot be clearly distinguished in the SEM images; instead, its presence can be inferred indirectly from the slight increase in fibre diameter and from the appearance of small surface irregularities surrounding the fibres. In images (G,H), a significant increase in surface roughness is evident, caused by the presence of MZP particles distributed unevenly on the fibre surface. These deposits generate localized microvoids, which may influence both mechanical properties and absorption behaviour. The fibres remain relatively uniform, albeit with irregular shapes and variable diameters ranging from 130 nm to 3 μm, and present larger aggregates compared with those observed for the undoped phosphate. As in the previous case, the thin phosphate coating itself is not directly resolvable by SEM, but its deposition contributes to the observed increase in fibre thickness and change in surface texture.

To confirm the coating process, the SEM images in Figure S2 illustrate MP (A,B), MLP (C,D), and MZP (E,F) deposits obtained using the MAPLE technique on silicon (Si) substrate. The silicon surface, being rigid and smooth, exhibits a different interaction with the deposited materials compared to PCL fibres. In images (A,B), the deposited layer appears relatively uniform, and characteristic of films obtained by MAPLE. In image (A), a transition edge between the substrate and the deposited layer can be distinguished, with variations in thickness across the surface; in image (B), very fine particles are visible over the entire surface. The surface appears relatively smooth, with small-scale, discontinuous deposits in certain regions. Compared to PCL fibres, this layer is more uniform, with finely dispersed particles forming a thin coating on the surface. In images (C,D), the layer is visibly rougher and more irregular, with elongated, acicular particles resembling needle-like structures, suggesting a significant modification in the crystallization process of lithium-doped material. Unlike the fibres, where particles were more uniformly distributed, both MLP and MZP exhibit irregular particle growth and deposition on the silicon substrate. In images (E,F), a rougher layer can be observed, consisting of larger spherical particles with less uniform coverage. On the silicon substrate, zinc doping promotes irregular particle growth, suggesting a tendency toward nucleation and faster, more pronounced crystal growth compared to undoped phosphate.

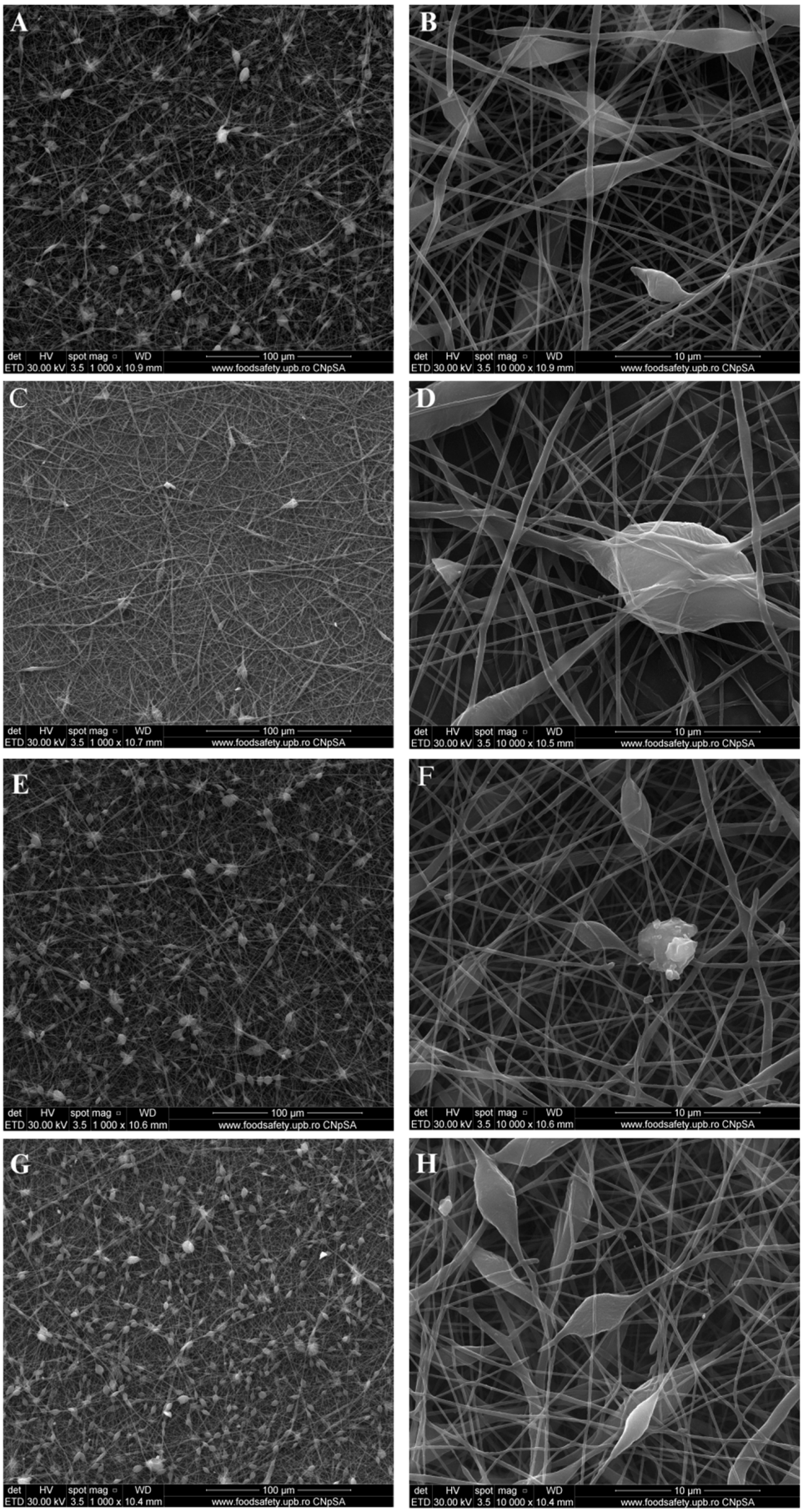


Figure 9. SEM images of fibres**:** (**A**,**B**) pure PCL, (**C**,**D**) PCL-MP, (**E**,**F**) PCL-MLP and (**G**,**H**) PCL-MZP.

To confirm the deposition of phosphate phases on the fibres surface, EDX spectroscopy and the corresponding elemental distribution maps were employed. Figure 10A highlights the intensities of the elements present in the material, with aluminium (Al) showing the highest concentrations. This can be attributed to the aluminium substrate on which the samples were placed, while the MAPLE technique may have influenced these values due to the reduced thickness and possible non-uniform distribution of the deposited layer on the fibre surface. The presence of carbon (C) and oxygen (O), elements characteristic of the polymer, is also observed, along with magnesium (Mg) and phosphorus (P), detected at higher concentrations in the case of MLP deposition. These variations may indicate a more efficient deposition or dispersion of the material, as well as more favourable evaporation during processing, compared to MP and MZP. The presence of iron (Fe), detected at low concentrations, may suggest contamination from the synthesis equipment or during sample preparation.

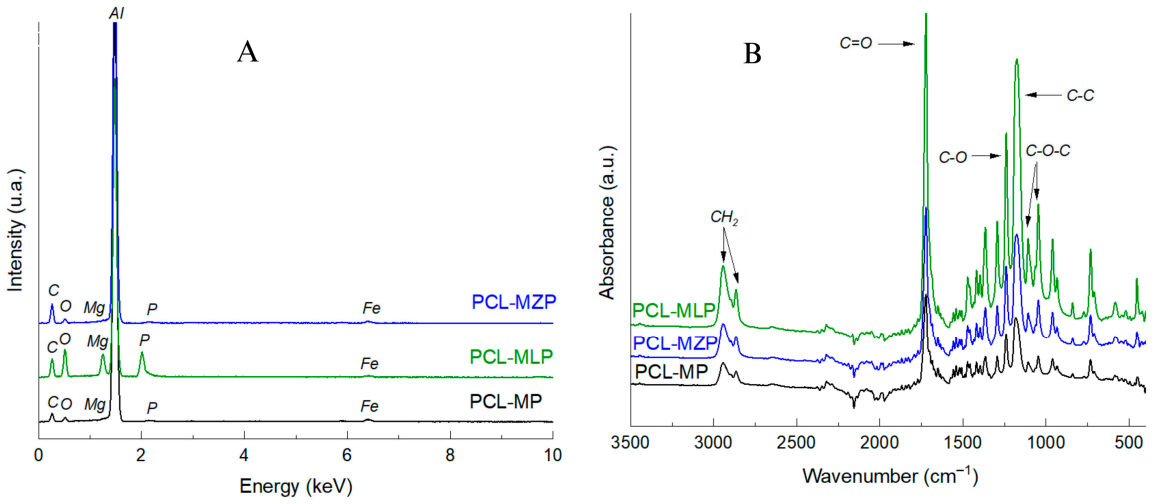


Figure 10. (**A**) EDX spectra and (**B**) ATR-FTIR spectra of PCL fibres coated using the MAPLE technique.

The ATR-FTIR shown in Figure 10B displays the characteristic PCL bands, confirming the presence of the polymeric matrix in all analysed samples. In the spectral region around 2956 cm^{-1}, 2926 cm^{-1}, and 2854 cm^{-1}, symmetric and asymmetric stretching bands of methylene groups (–CH_2–) can be observed, characteristic of the aliphatic chain of PCL [38,46]. The strong band at approximately 1732 cm^{-1} is attributed to the stretching vibration of the carbonyl (C=O) group, while the peak near 1240 cm^{-1} corresponds to C–C stretching in the ester structure [38]. Bands observed around 1293 cm^{-1} indicate C–O stretching vibrations, characteristic of the ester groups of PCL, whereas the spectral maxima near 1170 cm^{-1} are associated with symmetric C–O–C stretching vibrations [38]. These bands are well preserved in all three composites, indicating that the presence of phosphate phases does not significantly affect the chemical structure of the base polymer, as the deposited layer is very thin.

The analyses confirm the presence of characteristic elements in the obtained phosphate powders. All investigated samples exhibit a tendency toward particle agglomeration, accompanied by variations in elemental distribution, as observed in Figure 11. The high content of carbon (C) confirms the presence of the organic polymeric matrix, while magnesium (Mg), phosphorus (P), and zinc (Zn) are characteristic of the deposited phosphate phases. In the elemental maps, carbon (C) is represented in green and appears as the most intense and widespread signal due to the high concentration in the structure of PCL, oxygen (O) in blue, magnesium (Mg) in yellow, phosphorus (P) in purple, and zinc (Zn) in orange.

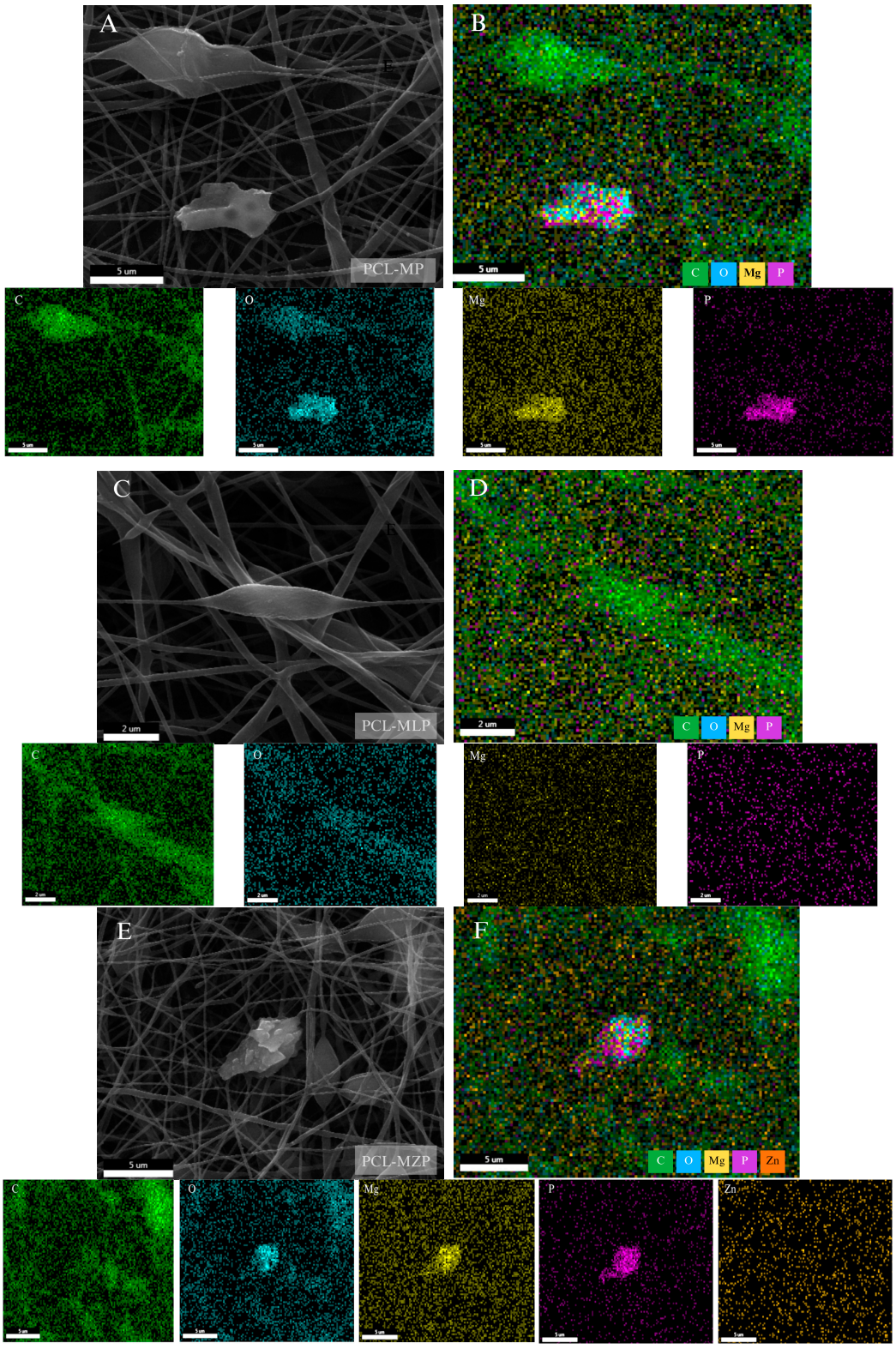


Figure 11. Elemental distribution maps of: (**A**,**B**) PCL-MP, (**C**,**D**) PCL-MLP and (**E**,**F**) PCL-MZP composite fibres.

Variations in colour intensity across the maps indicate differences in the local elemental concentration: brighter areas correspond to regions with higher signal intensity, typically associated with particle clusters, thicker fibre segments, or local accumulations of the phosphate coating. Darker regions reflect lower elemental content or thinner fibre areas. These variations are also influenced by the complex topography of the fibrous

network (overlapping fibres); surface roughness, and local thickness changes can affect the electron–matter interaction volume in EDX analysis.

3.2.2. Evaluation of Fiber Biodegradability

Figure 12 presents SEM images of PCL-MP (A,B), PCL-MLP (C,D), and PCL-MZP (E,F) fibres after immersion in SBF for 28 days. In images (A,B), a relatively uniform fibrous network can be observed. At higher magnification (B), the fibres exhibit roughened surfaces, local thickening, and irregular contouring. These morphological changes are characteristic of the degradation behaviour of PCL. As a bioresorbable polymer, PCL undergoes slow hydrolytic chain scission during prolonged exposure to SBF, which leads to surface erosion, swelling of fibre segments, and partial softening of the polymeric structure. Such processes typically result in the loss of the initially smooth fibre morphology and the emergence of uneven, thickened regions. Images (C,D) reveal more advanced degradation for the PCL-MLP fibres, including local flattening, surface roughness, and the appearance of microcracks. These features suggest increased brittleness caused by extended exposure to SBF rather than by the presence of lithium itself. Images (E,F) show the most pronounced degradation for the PCL-MZP fibres, with clear fibre fragmentation, collapse of certain fibre segments, and larger agglomerates of granular material. The formation of this porous surface layer is likely associated with the more intense SBF-induced erosion of the composite, as well as the presence of MZP particles on the fibre surface, which may contribute to local mechanical weakening. In both doping cases, the fibrous network becomes less uniform, indicating a stronger susceptibility of this composite to degradation processes during prolonged immersion in SBF.

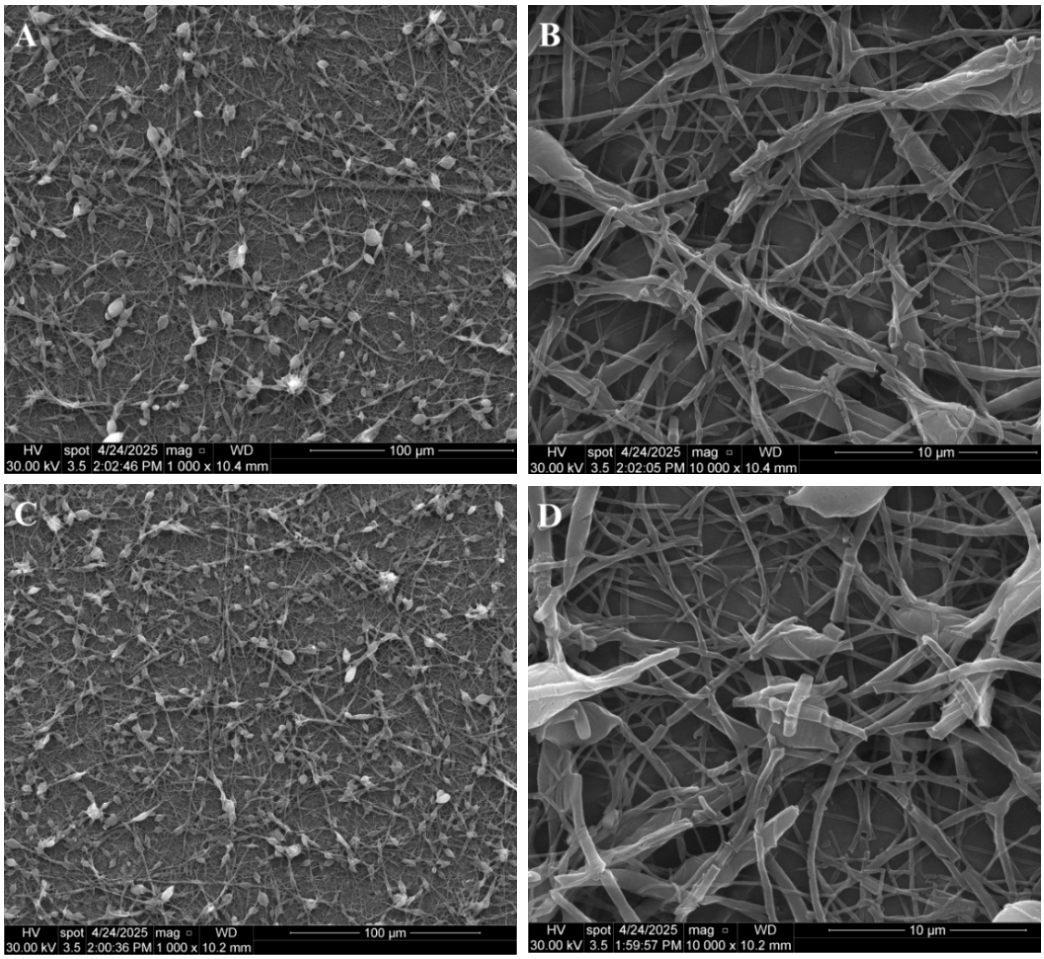


Figure 12. *Cont.*

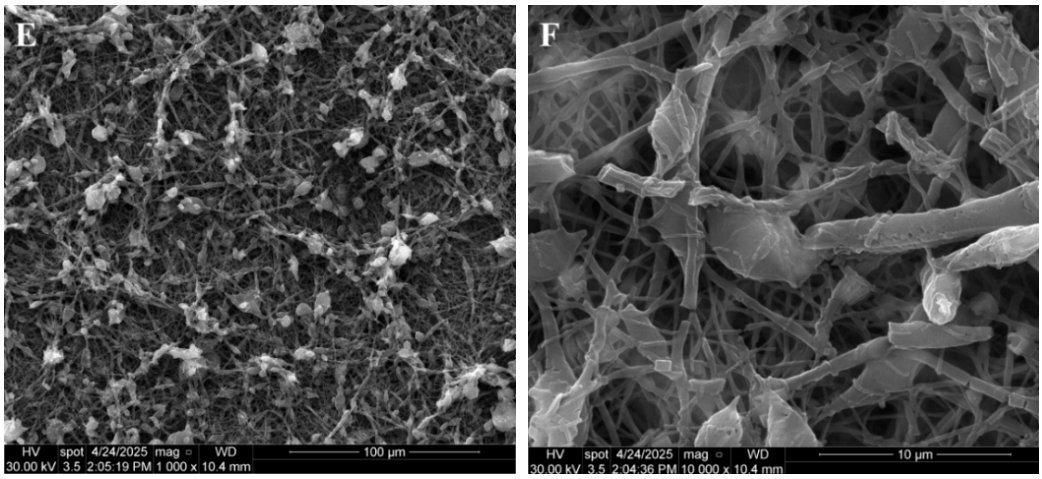


Figure 12. SEM images of fibres: (**A**,**B**) PCL-MP, (**C**,**D**) PCL-MLP and (**E**,**F**) PCL-MZP after immersion in SBF for 28 days.

3.2.3. Antibacterial Activity

Considering the antimicrobial properties established for MgP powders (Figures 7 and 8), the antibacterial properties of composite materials were qualitatively evaluated (Figure 13). This assessment was conducted through direct contact with a solid medium treated with *E. coli*, a microbial strain for which the MgP powders demonstrated moderate inhibitory effects.

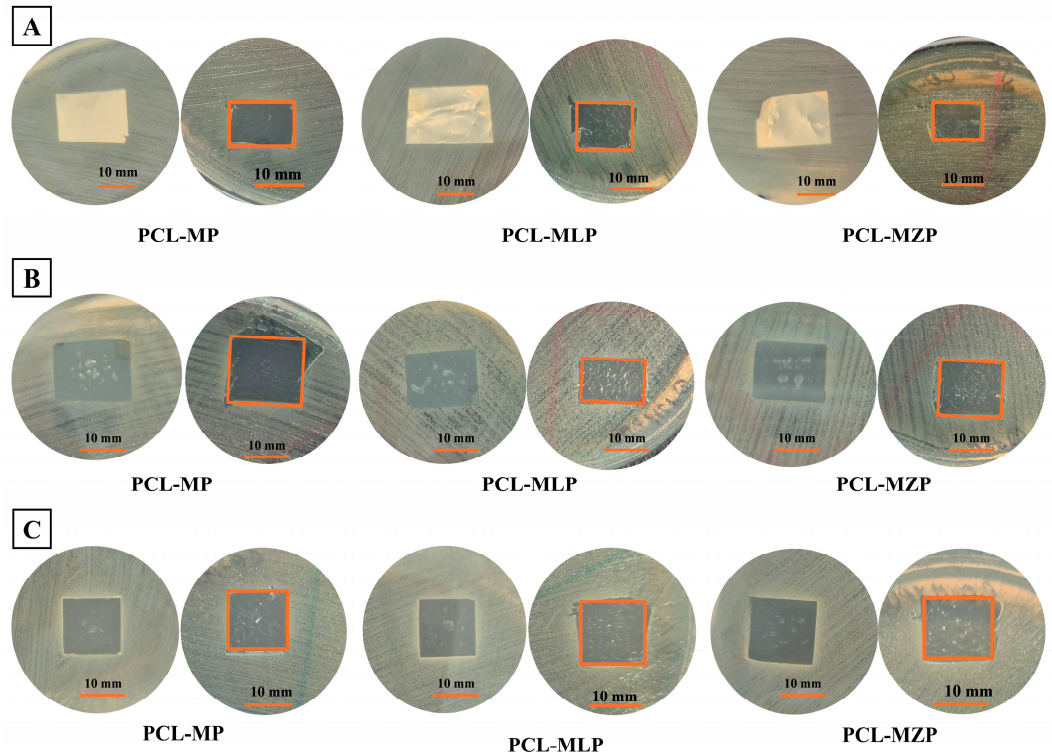


Figure 13. Influence of *E. coli* growth in the presence of PCL fibres on (**A**) aluminium, (**B**) silicon, and (**C**) glass substrate.

The images presented in Figure 13 suggest that no bacterial colony growth was observed in direct contact of the substrates treated with MgP powders with the solid medium. However, due to the very small amount deposited on the surface of the material, no inhibition zones were observed around the materials. This involves performing

additional analyses, from a quantitative point of view, especially of the antibiofilm activity of these composite materials.

3.2.4. Cell Viability—MTT Assay, Optical Microscopy and Fluorescence Microscopy

The conducted cell tests aimed to investigate the biological behaviour of the obtained composite materials. Figure 14 presents the results of the cell viability assay after 48 h of exposure. For the PCL-MP and PCL-MZP samples, a slight decrease in cell viability was observed but statistically significant only for PCL-MZP sample; however, the values did not exceed the cytotoxicity threshold, and all tested materials can be considered biocompatible, as they did not severely affect cell survival and remain within acceptable limits for biomedical applications. The PCL-MLP sample, in contrast, induced a significant increase in cell viability, reaching approximately 120%, suggesting an enhanced proliferative response of osteoblasts. This effect can be associated with the presence of lithium ions, which are known to significantly influence osteoblastic activity [11,15]. Studies have shown that lithium enhances osteoblast proliferation by activating the *Wingless/Integrated β-catenin signalling pathway* (Wnt/β-catenin), a key regulatory mechanism in bone formation that controls osteoblast proliferation, differentiation, and matrix production by stabilizing *β*-catenin and enhancing the expression of osteogenic genes [15]. Furthermore, low lithium concentrations have been reported to stimulate angiogenic and osteogenic gene expression, creating a more favourable environment for cell attachment and metabolic activity [19].

Figure 14 also illustrates the morphology of osteoblast cells on different substrates. On the control surface (A) and on PCL-MLP (F,G), the cells exhibit an elongated and well-defined morphology, indicating good adhesion and cellular proliferation, results that are well correlated to the viability assay. In contrast, on the PCL-MP (B,C) and PCL-MZP (D,E) substrates, cells appear more dispersed, sometimes with a rounded shape, and the cell density is visibly lower, which represents a similar trend to the results obtained by MTT assay. This difference may be attributed either to less populated regions within the microscopy field or to locally higher concentrations of zinc ions, which, although exhibiting significant antibacterial effects, can become cytotoxic at elevated doses [14,16]. Furthermore, some discrepancies between the two techniques (MTT and microscopy) are expected considering that MTT does not give a direct information on the number of cells but more on the metabolic activity of the cells, and in some cases we can see a decrease in the cell numbers but an increase in metabolic activity. These observations suggest a more favourable cell–substrate interaction in the case of lithium doping, as lithium ions are known to have beneficial effects on osteoblast activity and cellular differentiation [15,19].

The fluorescence microscopy images presented in Figure 14 support the findings of the MTT assay, showing that the composite materials do not exhibit cytotoxic effects. Clear differences in osteoblast behaviour can also be observed on the different substrates. On the control sample (A), the osteoblast cells display an elongated and uniformly spread morphology, with a well-organized actin filament network, indicating optimal adhesion. On the reference sample, namely pure PCL (B), cells are viable but show a more rounded shape and limited spreading. On the PCL-MP substrate (C), actin filament organization appears less developed, suggesting reduced cellular adhesion. In contrast, the PCL-MZP (D) and PCL-MLP (E) samples show markedly improved cell morphology, with osteoblasts displaying well-defined architecture and dense, organized actin structures, in agreement with the enhanced viability observed in the MTT assay and optical microscopy. The improved behaviour on the PCL-MZP fibres may be linked to the presence of zinc, as zinc is known to support cytoskeletal organization, promote

osteoblast adhesion, and stimulate proliferation at low concentrations, as reported in several studies [14,16–18]. For the PCL-MLP composite (E), the pronounced spreading and robust actin filament formation are consistent with the literature on lithium-based biomaterials, where lithium has been shown to enhance osteoblast attachment, migration, and cytoskeletal reorganization [16,19]. This pathway regulates genes involved in cell adhesion and cytoskeletal stability, which may explain the clear, elongated morphology observed in the fluorescence images. Such findings reinforce the idea that lithium can create a more favourable microenvironment for osteoblast–material interactions, supporting improved adhesion and early cytoskeletal maturation.

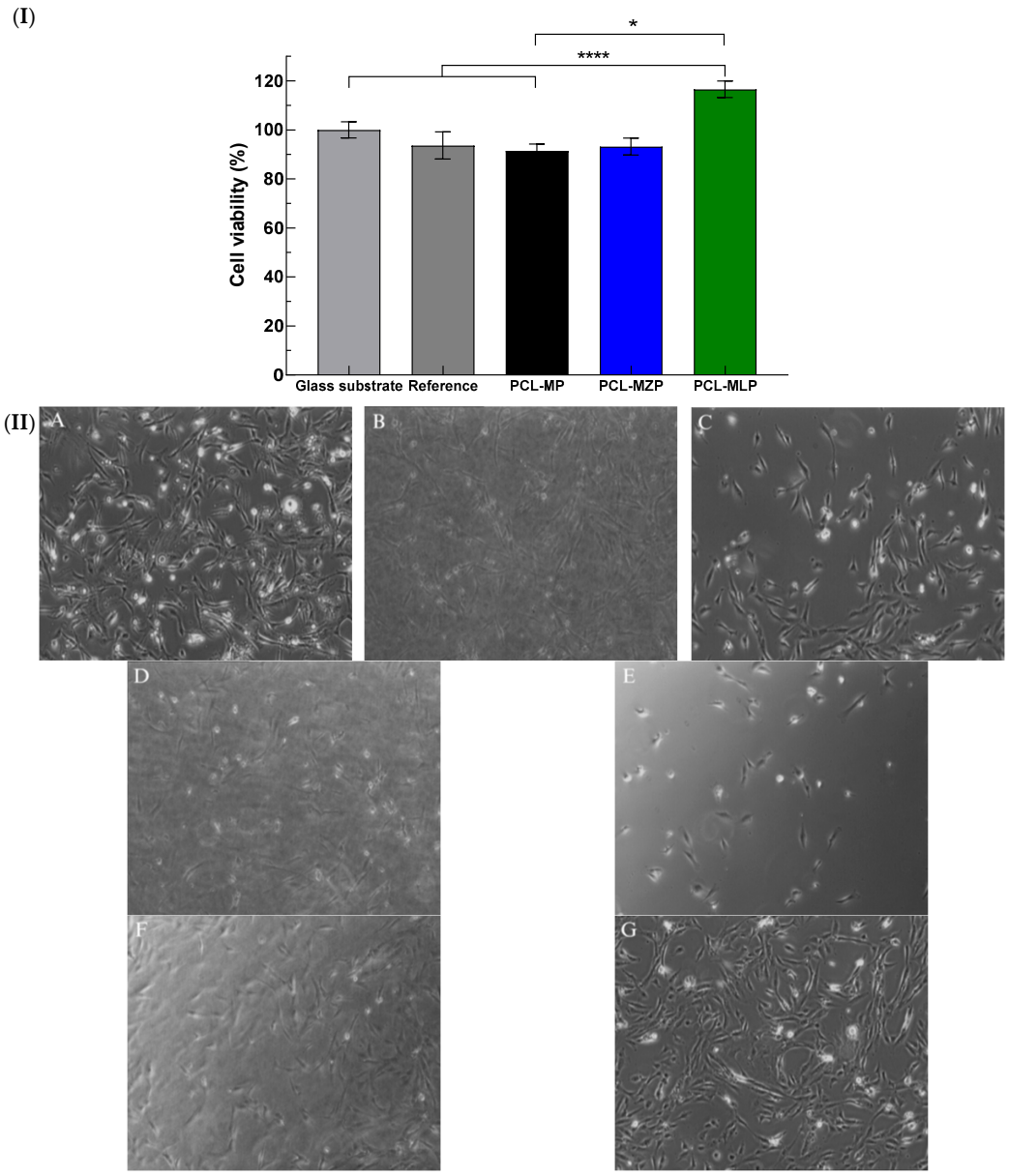


Figure 14. *Cont.*

(**III**)

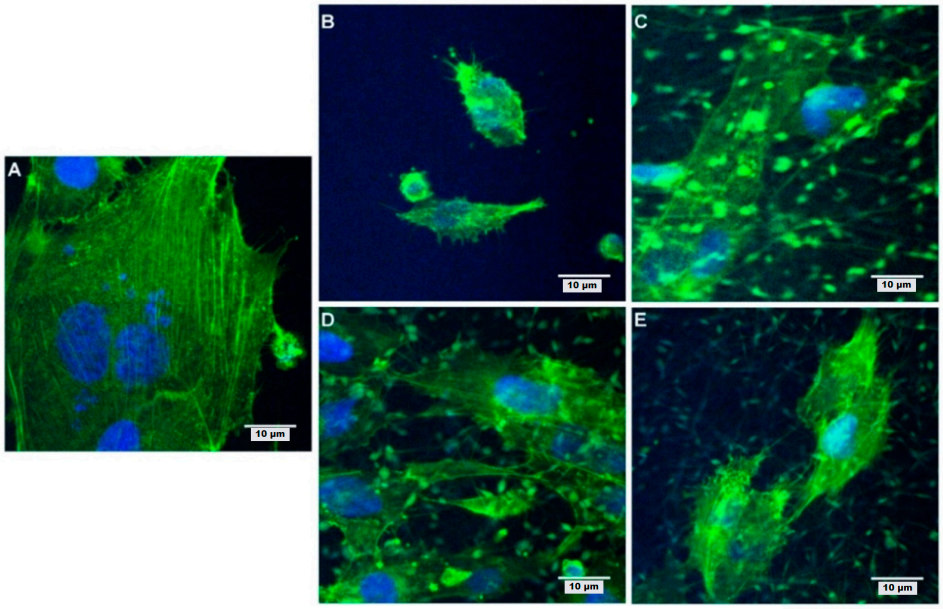


Figure 14. (**I**) Osteoblast cell viability in the presence of PCL fibres coated using the MAPLE technique. Data are represented as mean ±SD ($n = 3$). p values were calculated using one-way ANOVA analysis with Bonferroni's multiple comparison post-test. * $p < 0.05$, **** $p < 0.0001$. (**II**) Morphology of osteoblast cells in the presence of: (**A**) Control (glass), (**B**,**C**) PCL-MP, (**D**,**E**) PCL-MZP and (**F**,**G**) PCL-MLP. Images were acquired using a 10× objective. (**III**) Fluorescence microscopy images of osteoblast cells in the presence of: (**A**) Control (glass), (**B**) reference (pure PCL), (**C**) PCL-MP, (**D**) PCL-MZP and (**E**) PCL-MLP. The scale bar is 10 µm and is the same for all images.

4. Conclusions

In this study, electrospun poly(ε-caprolactone) (PCL) fibres were functionalized with lithium- and zinc-doped magnesium phosphate coatings using the Matrix-Assisted Pulsed Laser Evaporation (MAPLE) technique. This approach enabled the formation of a thin bioactive surface layer, promoting more rapid ion release compared to conventional systems in which the inorganic phase is embedded within the polymer matrix.

Thermal and structural analyses confirmed the formation of the magnesium pyrophosphate ($Mg_2P_2O_7$) phase after calcination, with doping inducing only subtle structural modifications without altering the overall crystallographic phase. Compared to conventional calcium phosphate-based materials, magnesium phosphate systems—particularly $Mg_2P_2O_7$—offer the advantage of more controllable degradation behaviour and enhanced biological activity associated with Mg^{2+} ion release. In addition, the pyrophosphate structure contributes to improved structural stability, enabling a balance between mechanical integrity and resorption, which is critical for trabecular bone regeneration.

The functional performance of the materials was strongly influenced by the type of dopant. Zinc-doped phosphate demonstrated pronounced antimicrobial activity, supported by the smallest CMI and MBEC values determined in microbiological assays. Biologically, both lithium and zinc improved cellular response, enhancing osteoblast adhesion and proliferation through the controlled release of bioactive ions, with lithium showing more favourable effects on cell behaviour compared to zinc.

Several limitations must also be acknowledged. The SBF test did not provide quantitative evidence of bioactivity or mineralization, likely due to the very thin coating obtained by MAPLE and the relatively short immersion period. Furthermore, the thin deposited layer limited the detection of phosphate-related signals and restricted the ability to directly correlate structure with biological performance. In addition, although dopant

effects were observed, the interpretation of lattice modifications remains indirect and would require more detailed crystallographic analysis.

Overall, while the results demonstrate the potential of $Mg_2P_2O_7$-coated PCL fibres as bioactive systems, further optimization of coating thickness, uniformity, and composition, together with quantitative biological and degradation studies, is necessary to fully validate their applicability as alternatives to conventional calcium phosphate-based scaffolds.

Supplementary Materials: The following supporting information can be downloaded at: https://www.mdpi.com/article/10.3390/jcs10050223/s1, Figure S1: SEM images of: (A and B) MP, (C and D) MLP and (E and F) MZP powders before thermal treatment; Figure S2: SEM images of: (A and B) MP, (C and D) MLP and (E and F) MZP deposits on silicon substrate.

Author Contributions: Conceptualization, O.M.C. and C.B.; methodology, O.M.C., C.M.D., G.P.-P., M.B., C.-I.I. and C.B.; investigation, O.M.C., C.M.D., G.P.-P., M.B., R.M., C.-I.I. and C.B.; resources, G.P.-P., M.B., C.-I.I., S.-I.J. and C.B.; writing—original draft preparation, O.M.C. and C.B.; writing—review and editing, O.M.C., M.B., C.-I.I. and C.B.; supervision, S.-I.J. and C.B. All authors have read and agreed to the published version of the manuscript.

Funding: This research received no external funding.

Data Availability Statement: The original contributions presented in this study are included in the article/Supplementary Material. Further inquiries can be directed to the corresponding author.

Acknowledgments: The authors are grateful to the Romanian Government for providing access to the research infrastructure of the National Center for Micro and Nanomaterials through the National Program titled "Installations and Strategic Objectives of National Interest". M.B. and R.M. acknowledge the financial support of the Core Program at IFIN-HH, Contract No. PN 23 21 02 02/2023.

Conflicts of Interest: The authors declare no conflicts of interest.

References

1. Mao, A.S.; Mooney, D.J. Regenerative medicine: Current therapies and future directions. *Proc. Natl. Acad. Sci. USA* **2015**, *112*, 14452–14459. [CrossRef]
2. Oryan, A.; Alidadi, S.; Moshiri, A.; Maffulli, N. Bone regenerative medicine: Classic options, novel strategies, and future directions. *J. Orthop. Surg. Res.* **2014**, *9*, 18. [CrossRef]
3. Yang, X.; Wang, Y.; Zhou, Y.; Chen, J.; Wan, Q. The Application of Polycaprolactone in Three-Dimensional Printing Scaffolds for Bone Tissue Engineering. *Polymers* **2021**, *13*, 2754. [CrossRef]
4. Puscasu, M.E.; Busuioc, C. Robocasting of Calcium Magnesium Silicate Based Scaffolds: Advancing 3D Printing for Biomedical Applications. *Rom. J. Mater. Rev. Romana Mater.* **2024**, *55*, 337.
5. Storti, G.; Lattuada, M. 8—Synthesis of bioresorbable polymers for medical applications. In *Bioresorbable Polymers for Biomedical Applications*; Woodhead Publishing: Cambridge, UK, 2017; pp. 153–179. [CrossRef]
6. Hajebi, S.; Nasr, S.M.; Rabiee, N.; Bagherzadeh, M.; Ahmadi, S.; Rabiee, M.; Tahriri, M.; Tayebi, L.; Hamblin, M.R. Bioresorbable composite polymeric materials for tissue engineering applications. *Int. J. Polym. Mater. Polym. Biomater.* **2020**, *70*, 926–940. [CrossRef]
7. Huo, F. Nanostructured Ha/Pla Composite Scaffold for Bone Repair of Martial-Arts-Induced Ankle Injuries and Its Mechanical Behavior. *Rom. J. Mater. Rev. Romana Mater.* **2025**, *44*, 303.
8. Devi, K.B.; Lalzawmliana, V.; Saidivya, M.; Kumar, V.; Roy, M.; Nandi, S.K. Magnesium Phosphate Bioceramics for Bone Tissue Engineering. *Chem. Rec.* **2022**, *22*, e202200136. [CrossRef]
9. Adam, R.V.S.; Barbilian, A. Utilization of New Biodegradable Materials (Mg-Ca Alloys) in Orthopedic Surgery. Biocompatibility. Ph.D. Thesis, Carol Davila University of Medicine and Pharmacy, Bucharest, Romania, 2017.
10. Alexe, A.-C.; Burduşel, A.-C.; Gaftonianu, Ş.; Oprea, O.; Popescu, R.; Truşcă, R.; Ficai, A.; Andronescu, E. Biomaterials Based on Hydroxyapatite, Cerium Oxide and Essential Oils. *Rom. J. Mater. Rev. Romana Mater.* **2025**, *11*, 25.
11. Muşat, D.-N.; Burduşel, A.-C.; Gaftonianu, Ş.; Ficai, A.; Oprea, O.; Popescu, R.; Truşcă, R.; Andronescu, E. Bioglass Functionalised with Essential Oils for Biomedical Applications. *Rom. J. Mater. Rev. Romana Mater.* **2025**, *55*, 11.

12. Gelli, R.; Ridi, F. An overview of magnesium-phosphate-based cements as bone repair materials. *J. Funct. Biomater.* **2023**, *14*, 424. [CrossRef] [PubMed]
13. Liu, H.; Wu, J.; Wang, S.; Duan, J.; Shao, H. Effect of Sr^{2+} on 3D gel-printed $Sr_{3-x}Mg_x(PO_4)_2$ composite scaffolds for bone tissue engineering. *Int. J. Miner. Met. Mater.* **2023**, *30*, 2236–2244. [CrossRef]
14. Sarkar, K.; Kumar, V.; Devi, K.B.; Ghosh, D.; Nandi, S.K.; Roy, M. Anomalous in vitro and in vivo degradation of magnesium phosphate bioceramics: Role of zinc addition. *ACS Biomater. Sci. Eng.* **2019**, *5*, 5097–5106. [CrossRef]
15. Farmani, A.R.; Salmeh, M.A.; Golkar, Z.; Moeinzadeh, A.; Ghiasi, F.F.; Amirabad, S.Z.; Shoormeij, M.H.; Mahdavinezhad, F.; Momeni, S.; Moradbeygi, F.; et al. Li-doped bioactive ceramics: Promising biomaterials for tissue engineering and regenerative medicine. *J. Funct. Biomater.* **2022**, *13*, 162. [CrossRef] [PubMed]
16. Dornelas, J.; Dornelas, G.; Rossi, A.; Piattelli, A.; Di Pietro, N.; Romasco, T.; Mourão, C.F.; Alves, G.G. The incorporation of zinc into hydroxyapatite and its influence on the cellular response to biomaterials: A systematic review. *J. Funct. Biomater.* **2024**, *15*, 178. [CrossRef]
17. Yu, Y.; Liu, K.; Wen, Z.; Liu, W.; Zhang, L.; Su, J. Double-edged effects and mechanisms of Zn^{2+} microenvironments on osteogenic activity of BMSCs: Osteogenic differentiation or apoptosis. *RSC Adv.* **2020**, *10*, 14915–14927. [CrossRef]
18. Wang, S.; Li, R.; Xia, D.; Zhao, X.; Zhu, Y.; Gu, R.; Yoon, J.; Liu, Y. The impact of Zn-doped synthetic polymer materials on bone regeneration: A systematic review. *Stem Cell Res. Ther.* **2021**, *12*, 123. [CrossRef]
19. He, F.; Yuan, X.; Lu, T.; Wang, Y.; Feng, S.; Shi, X.; Wang, L.; Ye, J.; Yang, H. Preparation and characterization of novel lithium magnesium phosphate bioceramic scaffolds facilitating bone generation. *J. Mater. Chem. B* **2022**, *10*, 4040–4047. [CrossRef]
20. Sikder, P.; Bhaduri, S.B.; Ong, J.L.; Guda, T. Silver (Ag) doped magnesium phosphate micro-platelets as next-generation antibacterial orthopedic biomaterials. *J. Biomed. Mater. Res. Part B Appl. Biomater.* **2019**, *108*, 976–989. [CrossRef]
21. El-Sayed, S.A.M.; ElShebiney, S.; Beherei, H.H.; Kumar, P.; Choonara, Y.E.; Mabrouk, M. Copper-doped magnesium phosphate nanopowders for critical size calvarial bone defect intervention. *J. Biomed. Mater. Res. Part B Appl. Biomater.* **2024**, *112*, e35376. [CrossRef]
22. Mousa, S. Study on synthesis of magnesium phosphate materials. *Phosphorus Res. Bull.* **2010**, *24*, 16–21. [CrossRef]
23. Epperson, A.W. The Pyrophosphate Method for The Determination of Magnesium and Phosphoric Anhydride. *J. Am. Chem. Soc.* **1928**, *50*, 321–333. [CrossRef]
24. Shao, H.; Zhang, Y.; Lin, T.; Peng, J.; Wang, A.; Yu, F.; Zhang, Z.; Wang, L. Effect of Mg^{2+} on porous $Mg_xCa_{3-x}(PO_4)_2$ composite scaffolds for bone engineering by 3D gel-printing. *J. Mater. Sci.* **2020**, *55*, 7870–7882. [CrossRef]
25. Alberto, L.; Kalluri, L.; Qu, J.; Zhao, Y.; Duan, Y. Influence of polycaprolactone concentration and solvent type on the dimensions and morphology of Electrosprayed particles. *Materials* **2023**, *16*, 2122. [CrossRef] [PubMed]
26. Nalbandian, M.J.C. Development and Optimization of Chemically-Active Electrospun Nanofibers for Treatment of Impaired Water Sources. Ph.D. Thesis, University of California, Riverside, CA, USA, 2014.
27. Florea, D.A.; Grumezescu, V.; Bîrcă, A.C.; Vasile, B.Ș.; Mușat, M.; Chircov, C.; Stan, M.S.; Grumezescu, A.M.; Andronescu, E.; Chifiriuc, M.C. Design, Characterization, and Antibacterial Performance of MAPLE-Deposited Coatings of Magnesium Phosphate-Containing Silver Nanoparticles in Biocompatible Concentrations. *Int. J. Mol. Sci.* **2022**, *23*, 7910. [CrossRef] [PubMed]
28. Cristescu, R.; Doraiswamy, A.; Socol, G.; Grigorescu, S.; Axente, E.; Mihaiescu, D.; Chrisey, D.B.; Moldovan, A.; Narayan, R.; Stamatin, I.; et al. Polycaprolactone biopolymer thin films obtained by matrix assisted pulsed laser evaporation. *Appl. Surf. Sci.* **2007**, *253*, 6476–6479. [CrossRef]
29. Golafshan, N. Towards 3D Fabrication of MgP-Based Mechanically Competent Implants for Bone Regeneration. Ph.D. Thesis, Utrecht University, Utrecht, The Netherlands, 2023.
30. Perumal, G.; Sivakumar, P.M.; Nandkumar, A.M.; Doble, M. Synthesis of magnesium phosphate nanoflakes and its PCL composite electrospun nanofiber scaffolds for bone tissue regeneration. *Mater. Sci. Eng. C* **2020**, *109*, 110527. [CrossRef]
31. Lei, B.; Gao, X.; Zhang, R.; Yi, X.; Zhou, Q. In situ magnesium phosphate/polycaprolactone 3D-printed scaffold induce bone regeneration in rabbit maxillofacial bone defect model. *Mater. Des.* **2022**, *215*, 110477. [CrossRef]
32. Labet, M.; Thielemans, W. Synthesis of polycaprolactone: A review. *Chem. Soc. Rev.* **2009**, *38*, 3484–3504. [CrossRef]
33. Kayan, G.Ö.; Kayan, A. Polycaprolactone Composites/Blends and Their Applications Especially in Water Treatment. *ChemEngineering* **2023**, *7*, 104. [CrossRef]
34. Ilie, C.-I.; Spoiala, A.; Chircov, C.; Dolete, G.; Oprea, O.-C.; Vasile, B.-S.; Crainiceanu, S.A.; Nicoara, A.-I.; Marinas, I.C.; Stan, M.S.; et al. Antioxidant, Antitumoral, Antimicrobial, and Prebiotic Activity of Magnetite Nanoparticles Loaded with Bee Pollen/Bee Bread Extracts and 5-Fluorouracil. *Antioxidants* **2024**, *13*, 895. [CrossRef]
35. Dumitru, C.D.; Ilie, C.-I.; Neacsu, I.A.; Motelica, L.; Oprea, O.C.; Ripszky, A.; Pițuru, S.M.; Bălașea, B.V.; Marinescu, F.; Andronescu, E. Antimicrobial Composite Films Based on Alginate–Chitosan with Honey, Propolis, Royal Jelly and Green-Synthesized Silver Nanoparticles. *Int. J. Mol. Sci.* **2025**, *26*, 6809. [CrossRef]
36. *CLSI M100*; Performance Standards for Antimicrobial Susceptibility Testing. CLSI Supplement M100–36th. Clinical and Laboratory Standards Institute: Wayne, PA, USA; p. 4362026.

37. Kokubo, T.; Takadama, H. How useful is SBF in predicting in vivo bone bioactivity? *Biomaterials* **2006**, *27*, 2907–2915. [CrossRef] [PubMed]
38. Harris, S.A.D.; Enger, R.J.; Riggs, L.B.; Spelsberg, T.C. Development and characterization of a conditionally immortalized human fetal osteoblastic cell line. *J. Bone Miner. Res.* **1995**, *10*, 178–186. [CrossRef] [PubMed]
39. Nord, A.G.; Kierkegaard, P. The crystal structure of $Mg_3(PO_4)_2$. *Acta Chem. Scand.* **1968**, *22*, 1466–1474. [CrossRef]
40. Mahajan, R.; Prakash, R.; Choudhary, R.J.; Phase, D.M. Structural, electronic and optical characterization of Eu^{3+}/Dy^{3+}single and co-doped $Mg_2P_2O_7$ phosphors. *Phys. Scr.* **2021**, *96*, 075808. [CrossRef]
41. Massit, A.; El Yacoubi, A.; Kholtei, A.; El Idrissi, B.C. XRD and FTIR analysis of magnesium substituted tricalcium calcium phosphate using a wet precipitation method. *Biointerface Res. Appl. Chem.* **2020**, *11*, 8034–8042. [CrossRef]
42. Mahajan, R.; Prakash, R. A review report on structural and optical characterization of rare earth/transition metal doped pyrophosphate phosphors. *J. Mater. Sci. Mater. Electron.* **2022**, *33*, 25491–25517. [CrossRef]
43. Krokhicheva, P.A.; Goldberg, M.A.; Fomin, A.S.; Khayrutdinova, D.R.; Antonova, O.S.; Baikin, A.S.; Leonov, A.V.; Merzlyak, E.M.; Mikheev, I.V.; Kirsanova, V.A.; et al. Zn-Doped Calcium Magnesium Phosphate Bone Cements Based on Struvite and Their Antibacterial Properties. *Materials* **2023**, *16*, 4824. [CrossRef] [PubMed]
44. Shannon Ionic Radii Database, Imperial College London. Available online: https://abulafia.mt.ic.ac.uk/shannon/ptable.php (accessed on 4 April 2025).
45. Doicin, I.E.; Golea, A.-D.; Neacsu, I.A.; Ene, V.L.; Bîrcă, A.C.; Holban, A.; Andronescu, E. Spin-Coating Deposition of Antimicrobial ZnO Nanoparticles on Cotton Fabrics for Medical Applications. *Rom. J. Mater. Rev. Romana Mater.* **2024**, *54*, 189.
46. Chen, C.; Liu, F.; Zhang, X.; Zhao, Z.; Liu, S. Fabrication, characterization and adsorption properties of cucurbit[7]uril-functionalized polycaprolactone electrospun nanofibrous membranes. *Beilstein J. Org. Chem.* **2019**, *15*, 992–999. [CrossRef] [PubMed]

Disclaimer/Publisher's Note: The statements, opinions and data contained in all publications are solely those of the individual author(s) and contributor(s) and not of MDPI and/or the editor(s). MDPI and/or the editor(s) disclaim responsibility for any injury to people or property resulting from any ideas, methods, instructions or products referred to in the content.